



Global atmospheric methanol emissions inferred from IASI satellite measurements and aircraft data

Jean-François Müller¹, Trissevgeni Stavrakou¹, Bruno Franco², Lieven Clarisse², Crist Amelynck¹, Niels Schoon¹, Bert W. D. Verreyken¹, Beata Opacka¹, Corinne Vigouroux¹, Emmanuel Mahieu³, Maria Makarova⁴, and Kimberly Strong⁵

¹Royal Belgian Institute for Space Aeronomy (BIRA-IASB), Avenue Circulaire 3, 1180, Brussels, Belgium

²Spectroscopy, Quantum Chemistry and Atmospheric Remote Sensing (SQUARES), Brussels Laboratory of the Universe (BLU-ULB), Université libre de Bruxelles (ULB), Brussels, Belgium

³Institut d'Astrophysique et de Géophysique, Université de Liège, Liège, Belgium

⁴Saint Petersburg State University, Atmospheric Physics Department, St. Petersburg, Russia

⁵Department of Physics, University of Toronto, Toronto, Canada

Correspondence: Jean-François Müller (jfm@aeronomie.be)

Abstract.

We employ an updated retrieval of space-based methanol (CH_3OH) column measurements from the Infrared Atmospheric Sounding Interferometer (IASI) and an emission optimisation framework built on the MAGRITTE chemical transport model to assess terrestrial emissions of methanol to the atmosphere between 2008 and 2019. We first carry out a IASI CH_3OH validation study based on concentration measurements from three airborne campaigns, using the model and the IASI averaging kernels to compute aircraft-based columns directly comparable to IASI data. IASI is found to underestimate high columns in the considered region. A linear regression gives $\Omega_{\text{IASI}} = 0.46\Omega_{\text{airc}} + 10.6 \cdot 10^{15} \text{ molec.cm}^{-2}$, with Ω_{IASI} and Ω_{airc} the IASI and aircraft-derived columns, respectively. Inverse modelling of terrestrial methanol emissions using MAGRITTE and bias-corrected IASI columns leads to much-improved overall agreement against in situ measurement campaigns and column data at eight FTIR stations. The optimised global biogenic methanol emissions ($\sim 160 \text{ Tg yr}^{-1}$) are 22–60% higher than previous top-down estimates, due to (1) column enhancements caused by the IASI bias-correction and (2) higher dry deposition velocities in the model over land, compared to previous model studies, based on a parametrisation constrained by extensive campaign data. The inversion results are less reliable over boreal forests due to shortcomings of both the bias-correction and the dry deposition scheme over these regions. The optimisation suggests large changes in the distribution and seasonality of emissions. Over tropical ecosystems, radiation and temperature appear to exert a stronger control on biogenic emissions than is currently accounted for in the MEGAN model.

1 Introduction

Methanol (CH_3OH) is, besides methane, the most abundant organic compound present in the atmosphere (e.g., Singh et al., 2001), due to its fairly long atmospheric lifetime, of the order of 5 days (Millet et al., 2008; Stavrakou et al., 2011; Bates et al., 2021) and to its large global production dominated by an important biogenic emission flux, of magnitude ($\sim 100 \text{ Tg yr}^{-1}$



globally) equivalent to 18–23% of the global isoprene source (e.g., Guenther et al., 2012; Wells et al., 2014; Sindelarova et al., 2022). Other methanol sources include minor contributions from vegetation fires and anthropogenic emissions, each of the order of 10 Tg yr^{-1} globally (e.g., Jacob et al., 2005); photochemical production ($\sim 30\text{--}60 \text{ Tg yr}^{-1}$, e.g. Stavrakou et al., 2011; Khan et al., 2014; Bates et al., 2021) from reactions of CH_3O_2 with organic peroxy radicals (Madronich and Calvert, 25 1990) and with the hydroxyl radical OH (e.g., Archibald et al., 2009); as well as a large and uncertain marine biospheric source (Heikes et al., 2002) of which global magnitude ($24\text{--}85 \text{ Tg yr}^{-1}$, e.g., Millet et al., 2008; Bates et al., 2021) is more than offset by ocean uptake ($38\text{--}101 \text{ Tg yr}^{-1}$).

The importance of methanol for atmospheric chemistry stems primarily from its main atmospheric sink, namely oxidation by OH (e.g., Millet et al., 2008), which is an important source of carbon monoxide and formaldehyde (Millet et al., 2006; Hu 30 et al., 2011; Wells et al., 2014) and has minor impacts on tropospheric ozone and the oxidizing capacity of the atmosphere (Tie et al., 2003; Read et al., 2015). Methanol is also removed from the atmosphere through wet scavenging and uptake by oceans (see above) and vegetated areas (Jacob et al., 2005).

The terrestrial biogenic emission of methanol is primarily associated with the growth of cell walls in plant leaves (Fall and Benson, 1996), while other processes such as grassland cutting (Davison et al., 2008) and plant decay (Warneke et al., 35 1999) also contribute but are considered minor. The emissions are dependent on leaf temperature and light, and are higher in young and growing leaves than in mature and senescent leaves (Nemecek-Marshall et al., 1995). The estimated global biogenic source of methanol, of the order of 100 Tg yr^{-1} according to the Model of Emissions of Gases and Aerosols from Nature version 2.1 (MEGANv2.1) (Guenther et al., 2012), agrees with top-down estimates constrained by in situ (primarily airborne) measurements (Millet et al., 2008; Bates et al., 2021) or spaceborne retrievals of CH_3OH columns from the Infrared 40 Atmospheric Sounding Interferometer (IASI, Razavi et al., 2011; Stavrakou et al., 2011). These results are also consistent with the total terrestrial surface source of methanol ($\sim 120 \text{ Tg yr}^{-1}$) estimated based on column data from the Tropospheric Emission Spectrometer (TES, Cady-Pereira et al., 2012; Wells et al., 2014). Nevertheless, the confrontation of models with satellite data suggest substantial deviations from the MEGANv2.1 distributions, such as large underestimations over semi-arid regions (shrubland and savannas), overestimations over rainforests over Central Africa and parts of Amazonia, and a shift of 45 the seasonal peak of biogenic emissions towards the spring at mid-latitudes (Stavrakou et al., 2011; Wells et al., 2012, 2014).

Top-down emission estimates based on satellite data bear uncertainties for several reasons. Firstly, although the IASI- and TES-based inverse modelling of emissions improved model comparisons against independent data (Stavrakou et al., 2011; Wells et al., 2014), significant underestimations persisted in comparisons with aircraft and ground-based measurements, suggesting potential biases in the satellite data. Recent studies showed that satellite retrievals may present biases with respect to 50 independent datasets, e.g. for HCHO from UV-Visible sensors (e.g., Zhu et al., 2016; Vigouroux et al., 2020; De Smedt et al., 2021; Müller et al., 2024) and for several organic compounds from IR sensors including acetone and carboxylic acids from IASI (Franco et al., 2019, 2020) and methanol and other species from the Cross-track Infrared Sounder (CrIS, Wells et al., 2025). The characterisation of satellite data biases can be used to derive bias-corrected datasets for use in inverse modelling, as has been done for HCHO and NO_2 (Oomen et al., 2024; Müller et al., 2024; Souri et al., 2025).



55 Secondly, potential inconsistencies between the vertical concentration profile from the model and assumed in the satellite retrieval might lead to biases in the comparison of total columns, due to vertical variations in the sensitivity of the chemical compound. This issue can be addressed through the application of averaging kernels (Eskes and Boersma, 2003), which were however not available in previous works based on methanol IASI retrievals.

Thirdly, the inverse modelling of terrestrial methanol emissions is sensitive to the representation of other key budget components. Although very uncertain, marine emissions have little relevance due to their very small impact over land (Bates et al., 60 2021). Of higher importance is the production due to the $\text{CH}_3\text{O}_2 + \text{OH}$ reaction, which was ignored in the earlier studies, including Stavrakou et al. (2011) and Wells et al. (2014). Most importantly, the parametrisation of methanol uptake on land surfaces was based on only few dry deposition data, despite the well-established bidirectional nature of biosphere/atmosphere exchange of methanol (Wohlfahrt et al., 2015). The adopted dry deposition velocities, typically below 0.6 cm s^{-1} (Jacob et al., 65 2005; Millet et al., 2008; Stavrakou et al., 2011), are significantly lower than average values reported in many field campaigns (Wohlfahrt et al., 2015). In some cases, the net methanol flux to the atmosphere is close to zero (Langford et al., 2010) or even negative during a large part of the year (Laffineur et al., 2012).

The present study aims to address the above issues in several ways. We present a newly developed version of the IASI CH_3OH retrieval, IASIv4, including several methodological advances, among which the provision of averaging kernels. Next, 70 we validate this product using aircraft measurements of methanol from several campaigns, and we use the results to propose a correction formula. The bias-corrected IASI dataset is then used to optimise terrestrial emissions in the global chemistry-transport model MAGRITTE (Müller et al., 2019). This model incorporates methanol formation due to $\text{CH}_3\text{O}_2 + \text{OH}$, as well as a detailed representation of methanol uptake. The deposition scheme over land is adjusted based on field campaign data. Finally, the optimisations are evaluated against a broad range of independent observations, including surface and airborne in 75 situ data as well as Fourier-transform infrared (FTIR) column measurements.

The manuscript is structured as follows. Sections 2.1–2.4 describe the IASIv4 retrieval, the airborne and surface in situ concentration datasets and the network of FTIR data. Section 2.5 provides a brief description of the MAGRITTE model focusing on the parametrisation of methanol sources and sinks; in particular, Sect. 2.5.5 and Appendix A describe the implementation of methanol dry deposition, including an evaluation of this scheme against observation-based estimates. Sections 2.6–2.7 present 80 the methodology used for IASI validation and for emission optimisation based on either aircraft or satellite data. Section 3 presents the evaluation of IASI biases using aircraft data, and proposes a bias-correction formula for use in inverse modelling. Section 4 presents an assessment of top-down terrestrial emissions based on IASI, while Section 5 provides an evaluation of the optimised results against independent data; finally, Section 6 presents the conclusions of this study.

2 Data and methods

85 2.1 IASI methanol columns

In this study, we use CH_3OH column measurements retrieved from infrared spectra recorded by IASI, which operates onboard the polar-orbiting MetOp series of meteorological satellites: MetOp-A (operational from 2007 to late 2021), MetOp-B (since



2013), and MetOp-C (since 2019). Each IASI sensor provides global coverage twice per day (\sim 9:30 local solar time, morning and evening overpasses) with a circular footprint of 12 km diameter at nadir. The dataset used here has been produced with 90 version 4 of the artificial neural network retrieval framework for IASI (ANNI). The IASIv4 CH_3OH product builds upon the previous ANNI-based CH_3OH dataset (v3) described in Franco et al. (2018) and incorporates the methodological advances introduced with the ANNI v4 retrieval framework (Clarissee et al., 2023). While these references provide a full description of the retrieval approach and resulting product, we summarize below the key aspects relevant for the present study.

First, the ANNI retrieval framework calculates for each IASI observation a hyperspectral range index (HRI), a sensitive metric 95 quantifying the strength of the signature of the target species in the spectrum. In ANNI v4, a regularization procedure in the HRI setup allows suppressing discrepancies that are due to changes in the instrument calibration and post-processing (Clarissee et al., 2023). This ensures HRI consistency throughout the full IASI time series and between the different IASI sounders. In a second step, for each IASI observation, the corresponding HRI is converted into a single-pixel gas total column (and uncertainty) using an artificial feedforward neural network (NN) trained to emulate the non-linear relationships between the HRI, 100 atmospheric and surface conditions, and the gas vertical abundance. The meteorological variables used as NN inputs (e.g., temperature profiles, water vapor content) are sourced from the hourly ERA5 reanalysis of the European Center for Medium-Range Weather Forecasts (ECMWF; Hersbach et al., 2020), co-located in space and time with the IASI measurements. Cloudy scenes are excluded from the retrievals, and post-retrieval quality filters reject unphysical results due to poor observational conditions 105 in which IASI cannot reliably measure the target gas (Franco et al., 2018; Clarisse et al., 2023). The single-pixel cloud flag used by the ANNI v4 framework is the NN-based cloud product developed specifically for IASI (Whitburn et al., 2022).

For its baseline retrieval, the ANNI framework assumes constant vertical profile shapes of the target gas, derived from model 110 simulations, with one representative profile over land and another over sea (Franco et al., 2018). For CH_3OH , these profile shapes have been updated in ANNI v4 to better match the average tropospheric CH_3OH vertical distribution inferred from the aircraft measurements described in Sect. 2.2. The updated ANNI v4 profile shapes are shown in Fig. 1 together with the globally averaged CH_3OH profiles from the MAGRITTE a priori simulation. Because these profile shapes can be a source of 115 retrieval errors, particularly when the assumed profile shape differs largely from the true gas vertical distribution, the ANNI v4 framework produces a total-column averaging kernel (AVK) for each retrieved gas column (Clarissee et al., 2023). These AVKs are useful for harmonizing vertical-profile assumptions when comparing IASI retrievals with independent observations or atmospheric model outputs. This can be achieved by applying the IASI AVKs to the external dataset to simulate what ANNIv4 would retrieve if it were to observe the modelled distributions. This is the approach adopted in this study. Another way to use 120 AVKs is by adjusting the IASI retrievals to match the vertical profile shape from the external dataset (see, e.g., Franco et al., 2024; Zhai et al., 2024). In addition, the ANNI v4 framework provides random and systematic uncertainty estimates associated with each retrieved column (Clarissee et al., 2023). It is worth noting that, as applying the AVKs removes the uncertainties on the assumed vertical CH_3OH distribution, the final product includes single-pixel uncertainty values both with and without accounting for the vertical-profile uncertainty terms. In this study, only the daytime measurements of the IASIv4 CH_3OH product are used, as these offer enhanced sensitivity to weak infrared absorbers such as CH_3OH .

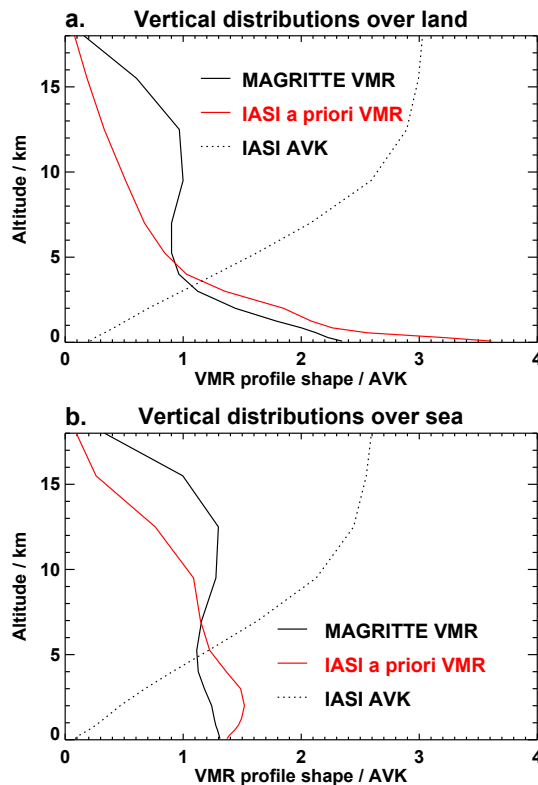


Figure 1. Average profile shapes of the methanol volume mixing ratio (VMR) and IASI total column averaging kernel (AVK) (a) over land, and (b) over sea. Red curves: CH_3OH mixing ratio profile shape used in the IASI retrieval. Black solid lines: globally-averaged profiles from the MAGRITTE model, for year 2008 (a priori simulation, see Sect. 2.5). Dotted line: globally-averaged IASI averaging kernel.

2.2 Aircraft concentration data

Table 1 lists the aircraft data used in this study. Three datasets from campaigns conducted over the United States in 2012–2013 are used to evaluate the IASI CH_3OH columns, as described in Sect. 2.6. Additional campaign datasets spanning 2008–2018 are used to evaluate the global inverse modelling results constrained by IASI. The campaigns are detailed below.

The DC3 (Deep Convective Clouds and Chemistry) mission took place over the Central U.S. in May–June 2012 (Barth et al., 2015). Methanol was measured from two aircraft, the NASA DC8 and the NSF/NCAR Gulfstream V (GV). Proton Transfer Reaction - Quadrupole Mass Spectroscopy (PTR-Q-MS) was employed on the DC8, whereas the Trace Organic Gas Analyzer (TOGA) from NCAR was used on the GV. SEAC⁴RS (Studies of Emissions, Atmospheric Composition, Clouds and Climate Coupling by Regional Surveys) was conducted over the southeastern U.S. in August–September 2013 on board the NASA DC8 aircraft (Toon et al., 2016). SENEX (Southeast Nexus) (Warneke et al., 2016) used the NOAA WP-3D aircraft to sample the lower troposphere (below ca. 6 km altitude) over the southeast USA in June 2013. ARCTAS (Arctic Research of the



Table 1. Aircraft campaign datasets in this work. The first three datasets are used to determine the CH₃OH biases through aircraft-based inversion (Sect. 2.6). All datasets are used to evaluate the emission inversions constrained by IASI. PTR-Q-MS: Proton Transfer Reaction - Quadrupole Mass Spectroscopy; PTR-ToF-MS: Proton Transfer Reaction - Time-of-Flight Mass Spectroscopy; TOGA: Trace Organic Gas Analyzer.

Aircraft dataset	Period	Measurement technique	Reference
SEAC ⁴ RS	Aug-Sep 2013	PTR-Q-MS	Wisthaler et al. (2002)
SENEX	Jun-Jul 2013	PTR-Q-MS	de Gouw and Warneke (2007)
DC3 (DC8)	May-Jun 2012	PTR-Q-MS	Wisthaler et al. (2002)
DC3 (GV)	May-Jun 2012	TOGA	Apel et al. (2003, 2010, 2015)
ARCTAS	Jun-Jul 2008	PTR-Q-MS	de Gouw and Warneke (2007)
ARCTAS	Jun-Jul 2008	TOGA	Apel et al. (2003, 2010, 2015)
GoAmazon IOP1	Feb-Mar 2014	PTR-Q-MS	Lindner et al. (1998)
KORUS-AQ	May-Jun 2016	PTR-ToF-MS	Müller et al. (2014)
ATom 1-4	Jul-Aug 2016	TOGA	Apel et al. (2003, 2010, 2015)
	Jan-Feb 2017		
	Sep-Oct 2017		
	Apr-May 2018		

Composition of the Troposphere from Aircraft and Satellites) took place in 2008 (Jacob et al., 2010). Two instruments, PTR-Q-MS and TOGA, were used to measure CH₃OH on the same platform. We used the June 2008 campaign, which mostly took place over California and surrounding oceanic regions, and the July 2008 campaign which mainly took place above Canada

135 (Fig. 2). GoAmazon (Observations and Modeling of the Green Ocean Amazon) was conducted around Manaus, Brazil, in the central Amazon basin in 2014–2015. It included ground measurements at several sites as well as aircraft observations from a G-159 Gulfstream I (G-1) mostly operated in the boundary layer and a Gulfstream G550 in the free troposphere. CH₃OH was measured on board the G-1 during the first Intensive Operating Period (IOP1) between 22 February and 23 March 2014.

140 KORUS-AQ (Korea-United States Air quality) investigated air composition with the NASA DC8 aircraft over Korea and surrounding areas in May–June 2016 (Crawford et al., 2021). The ATom (Atmospheric Tomography) mission (Brune et al., 2019; Wofsy et al., 2018) consisted of four separate campaigns, in July–August 2016, January–February 2017, September–October 2017, and April–May 2018. In each deployment, the NASA DC8 aircraft flew through the full lengths of the Pacific and Atlantic Oceans, between ca. 200 m and ~11 km altitude. TOGA was used to measure CH₃OH during these flights.

145 More details on the instrumental techniques are found in the references listed in Table 1. In all campaigns, we exclude data from urban plumes (identified as [NO₂] > 4 ppbv or [NO] > 0.5 ppbv) and biomass burning plumes ([CH₃CN] > 225 pptv). These filters remove only few data for most campaigns, e.g. 2%, 1% and 6% of measurements from SEAC⁴RS, SENEK and DC3, respectively, whereas a larger proportion of measurements (26%) was excluded due to fires from the ARCTAS-July campaign over Canada. The rationale for this filtering is that the missions often deliberately target urban or fire plumes (e.g.,

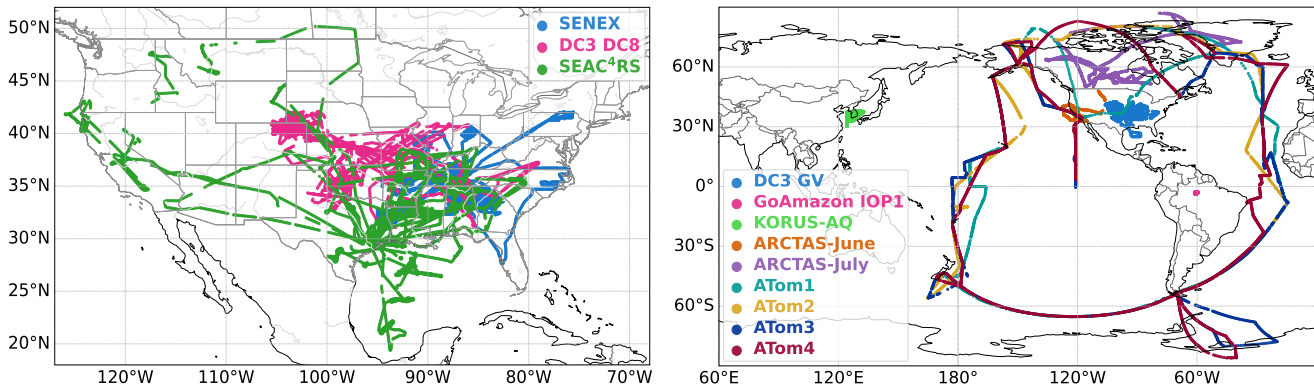


Figure 2. (Left) Flight tracks of the SENEX, DC3 (DC8), and SEAC⁴RS aircraft missions, used as constraints in the aircraft-based inversion over the U.S. (Right) Flight tracks of the additional aircraft campaigns used for model evaluation: DC3 (GV), GoAmazon, KORUS-AQ, ARCTAS, and ATom, cf. Table 1.

150 Jacob et al., 2010), leading to potential biases in comparisons with low-resolution model results. Measurements over ocean are also excluded, except for the ATom mission. The reported accuracy of CH₃OH measurements is ~20–25% for PTR-Q-MS (de Gouw and Warneke, 2007; Wisthaler et al., 2002), ~20% for TOGA (Apel et al., 2003), and ~5% for PTR-ToF-MS (Müller et al., 2014; Beaudry et al., 2025). The measurements are publicly available via data archive centers (see “Data availability” section). The flight tracks are shown in Fig. 2.

155 2.3 Other in situ methanol data

The averaged in situ methanol mixing ratios from measurement campaigns reported in 41 literature studies are listed in Table S1. The locations of the observations are provided in the Table and displayed on Fig. S1. Measurements conducted after 2019 or before 2008 are compared to climatological monthly values based on 2008–2019 optimisation results, whereas measurements performed within the study period (2008– 2019) are used for evaluation of IASI-based optimisation for the same 160 year. Various instrumental techniques were used to measure CH₃OH mixing ratios, among which PTR-Q-MS is the most common.

In addition to the sites of Table S1, we also use monthly CH₃OH concentrations measured by PTR-Q-MS at two sites in Belgium: the forested site of Vielsalm (50.305° N, 5.998° E) (Laffineur et al., 2012) and the cropland site of Lonzée (50.552° N, 4.746° E) (Bachy et al., 2018). The datasets of half-hourly mixing ratios and error estimates are publicly available (see “Data 165 availability” section). The 2- σ uncertainties (including statistical and systematic errors) are typically of the order of ~7%.



2.4 FTIR column data

The Network for the Detection of Atmospheric Composition Change (NDACC) Infrared Working Group (IRWG) operates a distributed set of more than twenty high-resolution FTIR spectrometers that record mid-infrared solar absorption spectra at high spectral resolution (De Mazière et al., 2018). Total columns and low-vertical-resolution profiles of many gases are 170 extracted from each spectrum by fitting modelled absorption to observed features using a radiative transfer forward model and an inversion (optimal estimation) retrieval.

Since methanol is not a mandatory NDACC target species, it is currently retrieved at only eight sites, listed in Table S2. This work uses data from all sites, namely Eureka, Canada, between 2008 and 2019; St Petersburg, Russia (2009–2019); 175 Toronto, Canada (2008–2019); Jungfraujoch (2008–2019); St Denis, Reunion Island (2009–2011); Maïdo, Reunion Island (2013–2019); Porto Velho, Brazil (2019); and Kitt Peak Observatory where methanol columns were measured between 1985 and 2003 (Rinsland et al., 2009). Unlike the official NDACC gases for which harmonized retrieval parameters are used within the network, individual sites have their own settings for methanol. Details on the retrieval methodology for each station can 180 be found in Rinsland et al. (2009) for Kitt Peak, Vigouroux et al. (2012) for St Denis (same settings used at Maïdo and Porto Velho), Viatte et al. (2014) and Wizenberg et al. (2024) for Eureka (same settings used at St Petersburg), Yamanouchi et al. (2023) for Toronto, and Bader et al. (2014) for Jungfraujoch. In addition to total columns, the FTIR retrievals provide vertical profiles. For methanol, the degrees of freedom for signal ranges between 1.0 and 1.8, with a good sensitivity from the ground up to 15 to 20 km depending on the site (see above references). The estimated random and systematic uncertainties for an individual methanol retrieval amount to 4–10% and 7–15%, respectively, also depending on the site.

2.5 Chemistry-transport model

185 2.5.1 General model description

We use the Model of Atmospheric composition at Global and Regional scales using Inversion Techniques for Trace gas Emissions (MAGRITTE v1.1), which calculates the distribution of 182 chemical species (Müller et al., 2019). The model is run 190 globally at $2^\circ \times 2.5^\circ$ resolution, with 40 vertical (σ -pressure) levels distributed between the surface and the lower stratosphere. The model incorporates a detailed description of the oxidation mechanism of biogenic volatile organic compounds (Müller et al., 2019). The chemical mechanism of anthropogenic and pyrogenic compounds is obtained from the IMAGES model (Stavrakou et al., 2009a; Bauwens et al., 2016). The photolysis rates are interpolated from tabulated values calculated using 195 the TUV photolysis estimation package (Madronich and Flocke, 1998). Meteorological fields are obtained from the ERA5 ECMWF reanalysis (Hersbach et al., 2020). The effect of diurnal variation on the photolysis rates and kinetic rate constants are considered through correction factors calculated from model simulations with a 20-min time step. These correction factors are used to calculate the diurnal cycle of CH_3OH concentrations required for comparisons with atmospheric measurements.

Anthropogenic emissions of CO, NO_x, SO₂, organic carbon and black carbon aerosols are taken from the HTAPv2 (Hemispheric Transport of Air Pollution version 2) inventory (Janssens-Maenhout et al., 2015). The speciated emissions of volatile organic compounds (VOCs) are obtained from the EDGARv4.3.2 inventory (Huang et al., 2017) between 2005 and 2012, and



are taken equal to their 2012 values afterwards. The anthropogenic methanol emission is taken equal to 67% of the HTAPv2
 200 total emission of alcohols. The resulting global flux is $10.5 \text{ Tg year}^{-1}$. Vegetation fire emissions are provided from the GFED4s
 database (van der Werf et al., 2017), with vertical injection profiles from Sofiev et al. (2013) and emission factors from Andreae
 and Merlet (2001). Biogenic VOC emissions of isoprene, monoterpenes and methanol are calculated using the MEGAN model
 (Guenther et al., 2012; Stavrakou et al., 2011) embedded in the MOHYCAN canopy environment model (Müller et al., 2008)
 205 driven by ERA5 meteorological fields and Leaf Area Index (LAI) data from MODIS Collection 6 reprocessed as described in
 Yuan et al. (2011).

Figure 3 displays the distribution of the major sources and sinks of methanol. Their estimation and implementation in
 MAGRITTE are described in the following subsections. Wet deposition, a minor methanol sink, is parametrised based on the
 cloud and precipitation ERA5 fields (Stavrakou et al., 2009c). This scheme distinguishes washout by convective precipitation,
 210 included in the convective transport scheme, from scavenging in and below large-scale stratiform clouds, which is represented
 as a first-order process. As in previous modelling studies, in-cloud oxidation of methanol is ignored, as it is considered very
 small (Jacob et al., 2005).

2.5.2 Photochemical production and sink

Methanol photochemical production proceeds primarily through the reactions of the methylperoxy radical with itself (CH_3O_2),
 with other (primary or secondary) organic peroxy radicals (RO_2) or with the hydroxyl radical (OH):



The rate and branching ratios of the self-reaction (R1–R2) are temperature-dependent (Burkholder et al., 2020). For the re-
 225 actions with other peroxy radicals (R3–R4), we follow Müller et al. (2019), the cross reaction rates being taken as twice
 the geometric mean of the self-reaction rates. The methanol-forming branching ratio usually ranges between 0.2 and 0.5 for
 primary and secondary peroxy radicals, and is equal to zero for tertiary and acyl peroxy radicals.

The reaction of CH_3O_2 with OH (R5–R7) is very fast (total rate of $1.6 \cdot 10^{-10} \text{ cm}^3 \text{ molec.}^{-1} \text{ s}^{-1}$, Assaf et al., 2016). It
 generates an activated trioxide that, for the most part, promptly decomposes into either methoxy and hydroperoxy radicals
 230 (R5) or methanol and O_2 (R6). A small fraction of the trioxide is stabilised (R7). The stabilised trioxide (denoted CH_3OOOH)
 undergoes atmospheric transport and further reactions, which might partly lead to secondary methanol formation (Müller et al.,

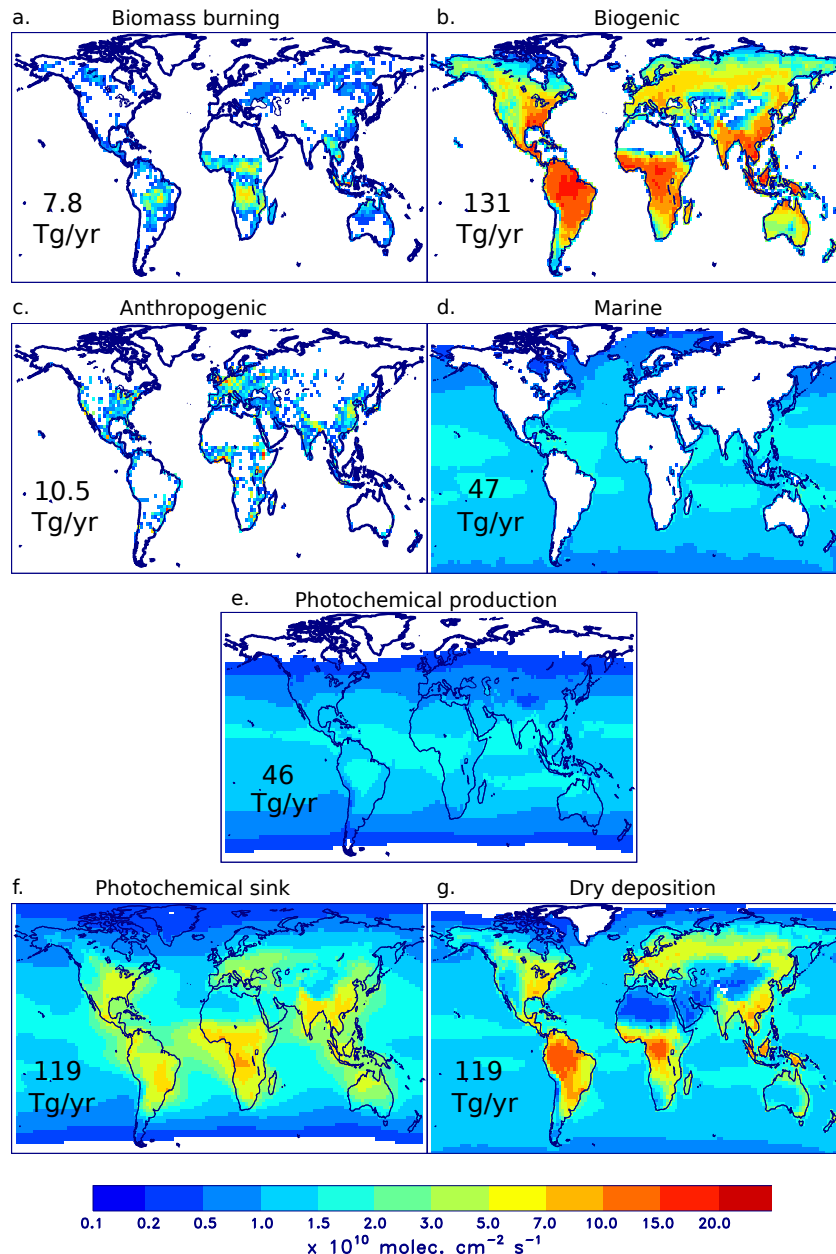


Figure 3. CH_3OH sources and sinks (a priori simulation, 2008–2019 average), in $10^{10} \text{ molec. cm}^{-2} \text{ s}^{-1}$. (a) Biomass burning, (b) biogenic source, (c) anthropogenic source, (d) marine source (gross flux), (e) photochemical production, (f) photochemical loss, and (g) dry deposition flux. The global emission or sink is given inset in each panel.

2016, 2019), although its fate is very uncertain. The stabilised fraction (R7) is ~ 0.1 near the Earth's surface, and decreases rapidly with altitude, due to an expected quadratic dependence on atmospheric pressure (Müller et al., 2016). The experimental



determinations of the R5 yield (0.9) at low pressure (Assaf et al., 2018) and of the methanol yield (0.06) at near-atmospheric pressure (Caravan et al., 2018) are consistent with the best theoretical estimate of the yields determined in Müller et al. (2016). For further details on the yields and chemical mechanism, we refer to Müller et al. (2019). At global scale, the MAGRITTE-calculated direct and indirect methanol yields from $\text{CH}_3\text{O}_2 + \text{OH}$ are 7.5% and 3.9%, respectively. The total average yield, 11.4%, is only slightly lower than the optimal value of 13% determined by Bates et al. (2021) using a global model and airborne methanol measurements from the ATom campaign. This discrepancy is very small in view of the large uncertainties, notably the possible role of water complexation on the reactions of CH_3O_2 radicals (Khan et al., 2015) and the fate of the stabilised trioxide (Caravan et al., 2018).

Reaction with OH is by far the main chemical sink of methanol in the atmosphere, proceeding at a rate ($k=2.9 \cdot 10^{-12} \exp(-345/T) \text{ cm}^3 \text{ molec.}^{-1} \text{ s}^{-1}$, Burkholder et al., 2020) resulting in a global lifetime against this process of about 10 days. Reaction of methanol with chlorine atoms is also considered ($k=5.5 \cdot 10^{-11} \text{ cm}^3 \text{ molec.}^{-1} \text{ s}^{-1}$, Burkholder et al., 2020) but is only a very minor sink globally (Müller et al., 2016; Bates et al., 2021).

2.5.3 Biogenic emission

The exchange of methanol between the terrestrial biosphere and the atmosphere is bidirectional. The biosphere is generally a net source under warm and sunny conditions, especially during springtime, while it is often a net sink under cold and humid conditions, e.g. during nighttime (e.g., Wohlfahrt et al., 2015). The net flux F ($\mu\text{g m}^{-2} \text{ h}^{-1}$) into the atmosphere above the canopy is expressed as

$$F = E - L, \quad (1)$$

where E is the emission rate, estimated using the MEGANv2.1 algorithm (Guenther et al., 2006; Stavrakou et al., 2011), and L is the uptake of methanol by vegetation. The uptake is calculated from the MAGRITTE-calculated above-canopy methanol concentration and a parametrisation of the dry deposition velocity (Sect. 2.5.5).

The emission rate is calculated in MEGANv2.1 as

$$E = C_{\text{CE}} \cdot \gamma_{\text{age}} \cdot \gamma_{\text{PT}} \cdot \text{LAI} \cdot \epsilon, \quad (2)$$

where C_{CE} is a normalization factor (=0.58), γ_{age} , γ_{SM} and γ_{PT} are dimensionless activity factors accounting for the emission dependence on respectively leaf age and environmental conditions, LAI is the leaf area index ($\text{m}^2 \text{ m}^{-2}$), and ϵ is the emission factor at standard conditions as defined in Guenther et al. (2006). On the basis of whole ecosystem flux measurements, ϵ has been set to $800 \mu\text{g m}^{-2} \text{ h}^{-1}$ for northern temperate and boreal broadleaf trees, needleleaf trees, shrubs and crops, and $400 \mu\text{g m}^{-2} \text{ h}^{-1}$ for grasses and other broadleaf trees. The distribution of Plant Functional Types (PFTs) is obtained from Guenther et al. (2006). γ_{age} is highest for young leaves, by a factor 3–3.5 relative to mature leaves (Stavrakou et al., 2011), and is parametrised as function of LAI temporal variations (Guenther et al., 2006). The temperature and light response function γ_{PT} includes the dependence of the emissions on leaf level temperature and visible radiation fluxes. It is expressed as

$$\gamma_{\text{PT}} = (1 - \text{LDF}) \cdot \gamma_{\text{T-li}} + \text{LDF} \cdot \gamma_{\text{P}} \cdot \gamma_{\text{T-ld}}, \quad (3)$$



where the LDF is the light-dependent fraction of the emissions at standard conditions, taken equal to 0.8 for methanol, $\gamma_{T\text{-li}}$ and $\gamma_{T\text{-ld}}$ are the temperature responses for respectively the light-independent and light-dependent fractions of the flux, and γ_P is the dependence on visible radiation of the light-dependent part. The activity factors for the light-dependent part are calculated using the isoprene algorithm of the MEGANv2.1 model, except that they do not incorporate a dependence on past temperatures.

270 Since leaf temperature and radiation fluxes are variable within the canopy, γ_{PT} is a weighted average of the expression given in Eq. 3, for all leaves. Leaf temperature and radiative fluxes are calculated separately for sunlit and shaded leaves at each of the 8 layers of the multi-layer canopy environmental model (Müller et al., 2008). For further details on biogenic methanol emission estimation, we refer to Müller et al. (2008) and Stavrakou et al. (2011).

275 The global biogenic methanol emission flux is here estimated at 130 Tg yr^{-1} , on average between 2008 and 2019. This agrees well with the MEGAN-MACC estimation (Sindelarova et al., 2014), but is significantly higher than other MEGAN-based estimations including Stavrakou et al. (2011) (105 Tg yr^{-1} for the year 2009) and the CAMS-GLOB-BIOv3.1 dataset (103 Tg yr^{-1} for 2000–2019, Sindelarova et al., 2022). Possible reasons include the higher LAI values of the reprocessed MODIS dataset (Yuan et al., 2011) (also adopted in CAMS-GLOB-BIO) compared to the dataset used by Stavrakou et al. (2011) and the higher surface areas of low-emitting PFTs (grassland and tropical broadleaf forests) in CAMS-GLOB-BIOv3.1, 280 compared to the MEGANv2.1 dataset (Guenther et al., 2006) used here.

2.5.4 Oceanic emission and oceanic uptake

As for the biosphere, the ocean-atmosphere exchange of methanol is bidirectional. The net flux ($\text{molec. cm}^{-2} \text{ s}^{-1}$) is written as a difference between a (gross) emission (E) and an uptake (U):

$$F = E - U = K_w (C_w - C_g \cdot H^{-1}), \quad (4)$$

285 where C_w and C_g (molec. cm^{-3}) are the methanol concentrations in water and in air, respectively,

$$H^{-1} = K_H RT \quad (5)$$

with K_H (M atm^{-1}) the Henry's law constant for methanol (Sander, 2015),

$$K_H = 200 \cdot \exp\left(5600\left(\frac{1}{T} - \frac{1}{298}\right)\right), \quad (6)$$

290 R the ideal gas constant ($=0.08205 \text{ L atm mol}^{-1} \text{ K}^{-1}$), and T the water temperature (in K). The conductance K_w is calculated by

$$K_w^{-1} = k_w^{-1} + (k_g H)^{-1}, \quad (7)$$

where k_w and k_g are the liquid phase and gas phase transfer velocity, respectively. As in Stavrakou et al. (2011), k_w is calculated as function of wind speed following Nightingale et al. (2000). The gas-phase transfer velocity is calculated using

$$k_g = (R_a + R_b)^{-1}, \quad (8)$$



295 where R_a and R_b are the aerodynamic and quasi-laminar layer resistances (s cm^{-1}), parametrised as discussed in Sect. 2.5.5. Note that the choice of Eq. 8 in place of the parametrisation of Johnson (2010) that was used in several previous global model studies (Millet et al., 2008; Stavrakou et al., 2011; Bates et al., 2021) has little impact on the calculated fluxes, as the globally-averaged k_g calculated using Eq. 8 is only about 3% lower than the corresponding value based on Johnson (2010).

300 The gross oceanic emission is proportional to the assumed oceanic subsurface concentration of methanol (C_w), for which we adopt the same value (118 nmol l^{-1}) as in several previous model studies (Millet et al., 2008; Stavrakou et al., 2011; Wells et al., 2014). This value was based on a single field study over the tropical Atlantic (Williams et al., 2004). As discussed by Bates et al. (2021), however, several recent field studies suggest significantly lower values. Furthermore, an average oceanic concentration of 61 nmol l^{-1} was inferred from an analysis of airborne CH_3OH measurements from the ATom campaign using the GEOS-Chem model (Bates et al., 2021), supporting the view that the concentration reported by Williams et al. (2004) was 305 likely not the most representative. This will have to be kept in mind when analyzing the methanol budget based on MAGRITTE.

As for biosphere-atmosphere exchanges, the oceanic uptake term (U) is calculated from the modelled near-surface CH_3OH concentration and a deposition velocity (cm s^{-1}) calculated (see Eq. 4) using

$$v_d = K_w \cdot H^{-1}. \quad (9)$$

2.5.5 Dry deposition

310 The dry deposition velocity is expressed (Wesely, 1989) as

$$V_d = \frac{1}{R_a + R_b + R_c} \quad (10)$$

with R_a the aerodynamic resistance between the surface and the first model level, R_b the quasi-laminar sublayer resistance, and R_c the bulk surface resistance. The parametrisations of the resistances R_a and R_b are obtained from the ECMWF Integrated Forecasting System (IFS) (ECMWF, 2021), as detailed in Appendix A. The surface resistance (s m^{-1}) is expressed (Zhang 315 et al., 2003) using

$$R_c = \left(\frac{1}{R_s + R_m} + \frac{1}{R_{ac} + R_g} + \frac{1}{R_{cut}} \right)^{-1}, \quad (11)$$

where R_s is the stomatal resistance, R_m the mesophyll resistance, R_{ac} the resistance to transfer in the canopy, and R_g is the resistance to soil uptake. Stomatal resistance being strongly radiation-dependent (Gao and Wesely, 1995), the conductance $\frac{1}{R_s + R_m}$ is calculated as a sum of contributions from each of the 8 layers of the canopy environmental model (Müller et al., 320 2008). The parametrisation of stomatal resistance is detailed in Appendix A. The parametrisation of the resistance R_{ac} depends on friction velocity, LAI and the plant functional type (Zhang et al., 2003).

The parametrisation of the other resistances of Eq. 11 is adapted from Wesely (1989) and Zhang et al. (2002). The conductances are expressed as linear combinations of the conductances for SO_2 (template for water-soluble species) and O_3 (for very



reactive species):

$$325 \quad \frac{1}{R_m} = \frac{K_H \cdot f_1}{3000} + 100 \cdot f_0 \quad (12)$$

$$\frac{1}{R_g} = \frac{K_H \cdot f_1}{10^5 \cdot R_g^{\text{SO}_2}} + \frac{f_0}{R_g^{\text{O}_3}} \quad (13)$$

$$\frac{1}{R_{\text{cut}}} = \frac{K_H \cdot f_1}{10^5 \cdot R_{\text{cut}}^{\text{SO}_2}} + \frac{f_0}{R_{\text{cut}}^{\text{O}_3}} \quad (14)$$

where f_0 and f_1 are species-dependent parameters, while $R_g^{\text{SO}_2}$, $R_g^{\text{O}_3}$, $R_{\text{cut}}^{\text{SO}_2}$ and $R_{\text{cut}}^{\text{O}_3}$ are soil uptake and cuticular resistances for SO_2 and O_3 (see Appendix A). f_0 is equal to 1 for very reactive species (e.g. ozone), and takes low values for weakly reactive compounds. In the original formulation of Wesely (1989), the f_1 factor was absent, i.e. their $f_1 = 1$. The formulation of Zhang et al. (2002) implies a value of $f_1 \sim 300$ for methanol at 298 K, whereas their $f_0 = 0.1$. Note that the precise values of f_0 and f_1 are unimportant for the mesophyll resistance, as long as f_1 is not much lower than 1.

Field measurements of methanol fluxes over vegetated areas generally indicate strong deposition in humid conditions, indicating that methanol is consumed in water films present in the soil and/or on leaves, even though the precise mechanisms responsible for methanol degradation in water are not fully elucidated (Laffineur et al., 2012; Wohlfahrt et al., 2015). This suggests that the high water-solubility of methanol plays a key role in determining its deposition, i.e. that the K_H term is dominant in the resistance expressions of Eqs. 12-14. Here, we adopt a high value of f_1 (=600) based on an evaluation of the dry deposition scheme against deposition velocities estimated from flux measurement campaigns at 13 sites, among which 8 temperate or boreal forest sites, 2 tropical forest sites, and 3 sites at other temperate ecosystems (Table S3). We adopt $f_0 = 1$, but as expected, this parameter has only a very minor impact within its expected range (0–1).

At 9 out of the 13 studies, night-time deposition velocities are reported, while 24-hour averages are estimated at the other sites. The meteorological fields used in the deposition scheme are obtained from hourly ERA5 fields for the months and years of the campaign measurements, except at one site (Blodgett in 1999) for which 2003–2013 averages are used. We use the LAI values reported for each site, when available, or from the MODIS Collection 6 dataset (at 0.5° spatial resolution) used in MAGRITTE. Table S3 and Fig. 4 summarize the model evaluation. On average, the model performs very well, with a negative bias of only 7% against the average observed v_d for all sites (0.82 cm s^{-1}). The model correlates well with the observations (Pearson's coefficient of 0.72) and most model predictions fall within 40% of the measurements. One notable exception is a coniferous forest site in Finland, where the model value (1.34 cm s^{-1}) overestimates the measurement-based v_d (0.3 cm s^{-1}) (Rantala et al., 2015) by a large factor, for reasons unclear. Part of the discrepancy might be due to the model calculating v_d at the first model layer ($\sim 10 \text{ m}$ above the surface), i.e. well below the highest measurement altitude (67 m). More work would be needed to investigate the reasons for this difference. At the other sites, part of the variability between the sites appears related to the role of humidity: the highest v_d ($\sim 1.5 \text{ cm s}^{-1}$) are observed (and modelled) at very humid forest sites (Vielsalm, Blodgett and Duke forest), whereas very low v_d values ($\sim 0.3 \text{ cm s}^{-1}$) are found at drier locations (Bosco Fontana, Italy and Ozarks, Missouri). The distribution and seasonal variation of the calculated deposition velocities for 2013 are displayed on Fig. S2.

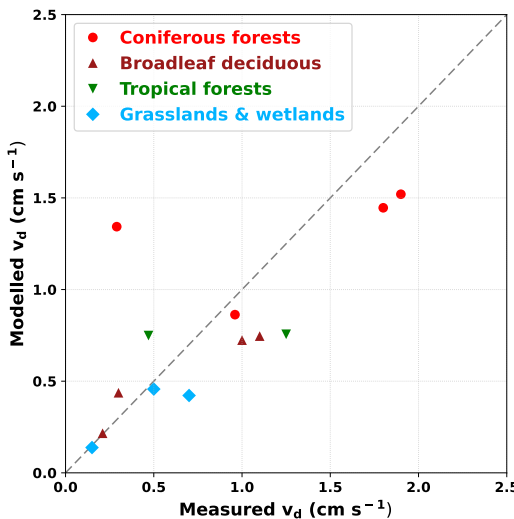


Figure 4. Scatter plot of observed and modelled CH_3OH dry deposition velocity in cm s^{-1} . The locations of the dry deposition measurement campaigns, dominant plant functional types, site coordinates, leaf area index, observed and simulated dry deposition velocities, and the corresponding references are summarised in Table S3. The symbols refer to the type of biome, coniferous (red circles), broadleaf deciduous (brown triangles), tropical forests (green triangles) and grasslands and wetlands (blue diamonds).

355 2.6 Inversion based on aircraft data

Similar to our previous work aimed at validating spaceborne HCHO columns using aircraft in situ data, the MAGRITTE model and its inverse modelling capability are used to generate CH_3OH model distribution closely approximating aircraft observations from three campaign datasets over the U.S. (Table 1). The methanol emissions used in the model are adjusted in order to minimise a cost function (J) quantifying the discrepancy between model and data,

$$360 \quad J(\mathbf{f}) = \frac{1}{2} [(\mathbf{H}(\mathbf{f}) - \mathbf{y})^T \mathbf{E}^{-1} (\mathbf{H}(\mathbf{f}) - \mathbf{y}) + \mathbf{f}^T \mathbf{B}^{-1} \mathbf{f}], \quad (15)$$

where \mathbf{f} is the vector of emission parameters, $\mathbf{H}(\mathbf{f})$ is the model operator acting on \mathbf{f} , \mathbf{y} is the observation vector, and \mathbf{E} and \mathbf{B} are the covariance matrices of the errors on the observations and the emission parameters, respectively. \mathbf{y} and $\mathbf{H}(\mathbf{f})$ are campaign-averaged mixing ratios at each model pixel ($2^\circ \times 2.5^\circ$) for which observations are available. The model averages are based on model values at the same times and locations as the measurements.

365 The monthly averaged emission from either anthropogenic, pyrogenic or biogenic category is expressed as

$$G(\mathbf{x}, t, \mathbf{f}) = \sum_{j=1}^m \exp(f_j) \phi_j(\mathbf{x}, t) \quad (16)$$



where ϕ_j denotes the a priori emission at a single pixel and month. The emission at a given pixel is not optimised when its maximum value over the course of the year is lower than a threshold of 10^9 molec. $\text{cm}^{-2} \text{s}^{-1}$, which is sufficiently low that the emission of most pixels are optimised over the contiguous U.S.

370 The matrix \mathbf{E} is assumed diagonal. The total uncertainty is obtained by quadratically adding a 20% relative uncertainty corresponding to the instrumental uncertainty (see Sect. 2.2) and a 200 pptv absolute error. The latter is higher than the limit of detection (100 pptv, Wisthaler et al., 2002) but gives more weight to higher CH_3OH abundances in the cost function.

375 The errors on all emission parameters are assumed to be a factor of 3. Anthropogenic emission parameters from pixels in the same country are weakly correlated (coefficient of 0.1), whereas parameters for different countries are not correlated. For biogenic and pyrogenic emissions, a decorrelation length of 500 km is used. The cost function is minimised using an quasi-
375 Newton optimisation algorithm involving the calculation of the gradient of the cost function by the adjoint of the model. The iterative search for the minimum is stopped when the norm of the gradient of the cost J is decreased by a factor of 30. This criterion is generally reached after 20 iterations.

380 Simulations start on July 1st 2011 and last 2.5 years. The optimised CH_3OH distributions are used to calculate, for each campaign, a campaign-average gridded column distribution accounting for the sampling times and averaging kernels of the IASI retrievals. Those columns are evaluated against the corresponding IASI columns at the locations of the aircraft measurements aggregated onto the model grid. Model pixels with less than 30 IASI measurements, or less than 10 aircraft measurements are excluded from analysis.

2.7 Inversion based on satellite data

385 The methodology presented in the previous section is used to optimise terrestrial methanol emissions at the global scale, based on monthly-average bias-corrected CH_3OH columns gridded at the model resolution ($2^\circ \times 2.5^\circ$). Since our focus is on terrestrial emissions, we exclude IASI data over oceans. In addition, we filter out very uncertain data (relative retrieval error larger than 100%) as well as low CH_3OH monthly columns ($< 10^{16}$ molec. cm^{-2} after bias correction) for which the IASI bias is not well characterised (see Sect. 3). Although the fluxes from three emission categories are inferred simultaneously, their distinction is uncertain. The biogenic flux being strongly dominant, the optimisation is not expected to provide much constraint on the 390 other categories (anthropogenic and pyrogenic), except at few locations/times such as large fire events. Another limitation of the framework stems from uncertainties in methanol losses, in particular the dry deposition sink of which the spatial distribution over land resembles that of the biogenic emission (Fig. 3). Marine methanol exchanges and the photochemical production have also their uncertainties, but their impact on top-down terrestrial emissions should be limited due to their minor relevance for methanol columns over source regions (Bates et al., 2021).

395 Separate inversions are performed for each year between 2008 and 2019, and each simulation starts on July 1st of the year preceding the target year. For consistency between the different years and with the validation exercise, we use only IASI data from MetOp-A. The IASI column uncertainty is obtained by quadrature addition of the IASI retrieval uncertainty and an absolute error taken to be $15 \cdot 10^{15}$ molec. cm^{-2} . The retrieval error (for monthly averaged columns at the model resolution) falls typically within the 5–15% range in tropical regions and in summer at mid-latitudes, but reaches $\sim 20\%$ at mid-latitudes during

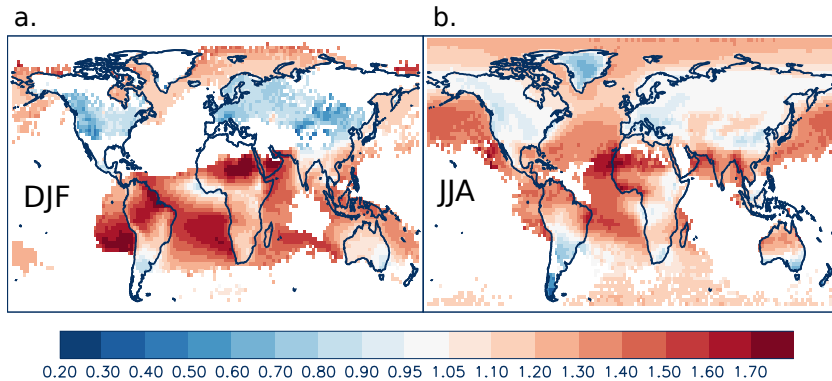


Figure 5. Ratio of the seasonally-averaged methanol columns from the prior simulation (2008–2019 average), calculated with averaging kernels, by the values calculated without averaging kernels. (a) December–January–February, (b) June–July–August.

400 winter and even higher values over snow-covered areas. The MAGRITTE monthly-averaged columns are calculated from daily values accounting for the number of measurements and averaging kernels for each day and for the sampling time ($\sim 9:30$ LT) of observations. Figure 5 illustrates the impact of averaging kernels on the modelled columns. Over tropical regions, the application of averaging kernels increases the columns, by up to 70%, likely due to the mixing of lower tropospheric methanol to higher altitudes promoted by deep convection. The opposite effect is evident at mid-latitudes during boreal winter, where 405 decreases reaching a factor of 2 are found in remote continental areas.

3 IASIv4 CH_3OH evaluation against aircraft-constrained model columns

Here we evaluate IASI against aircraft data, using MAGRITTE as transfer standard. Figure 6 illustrates the geographical distribution of vertically-averaged CH_3OH mixing ratios from the three campaigns. By far the highest values were observed during SENEX, largely because of the higher proportion of low-altitude measurements in this campaign (72% below 1.5 km) 410 compared to DC3 (15%) and SEAC⁴RS (35%). The vertical distribution of methanol (Fig. 7) shows indeed a maximum (ca. 4–7 ppbv) in the boundary layer, and a substantial decline in the free troposphere, down to 1–2 ppbv above 6 km, a feature well reproduced by the model. However, the simulation using a priori emissions underestimates the observations by ~ 20 –50% during SENEX and DC3. During SEAC⁴RS, model overestimations are seen over the southeast, and underestimations elsewhere. The largest underestimations are found over the U.S. midwest, reaching a factor of ~ 3 during DC3 and SEAC⁴RS 415 (Fig. 6). Similar, or even larger underestimations were obtained in previous model evaluations against aircraft campaigns over western U.S. (Stavrakou et al., 2011; Wells et al., 2014; Chen et al., 2019).

The optimised model using adjusted CH_3OH emissions reproduces very well the observations (Fig. 6–7), with spatial correlation coefficients of 0.97–0.98 for all campaigns, and negative biases of 1–3% for SENEX and SEAC⁴RS, and 7.5% for DC3. This agreement is achieved through a substantial increase of summertime methanol emissions over the western U.S.,

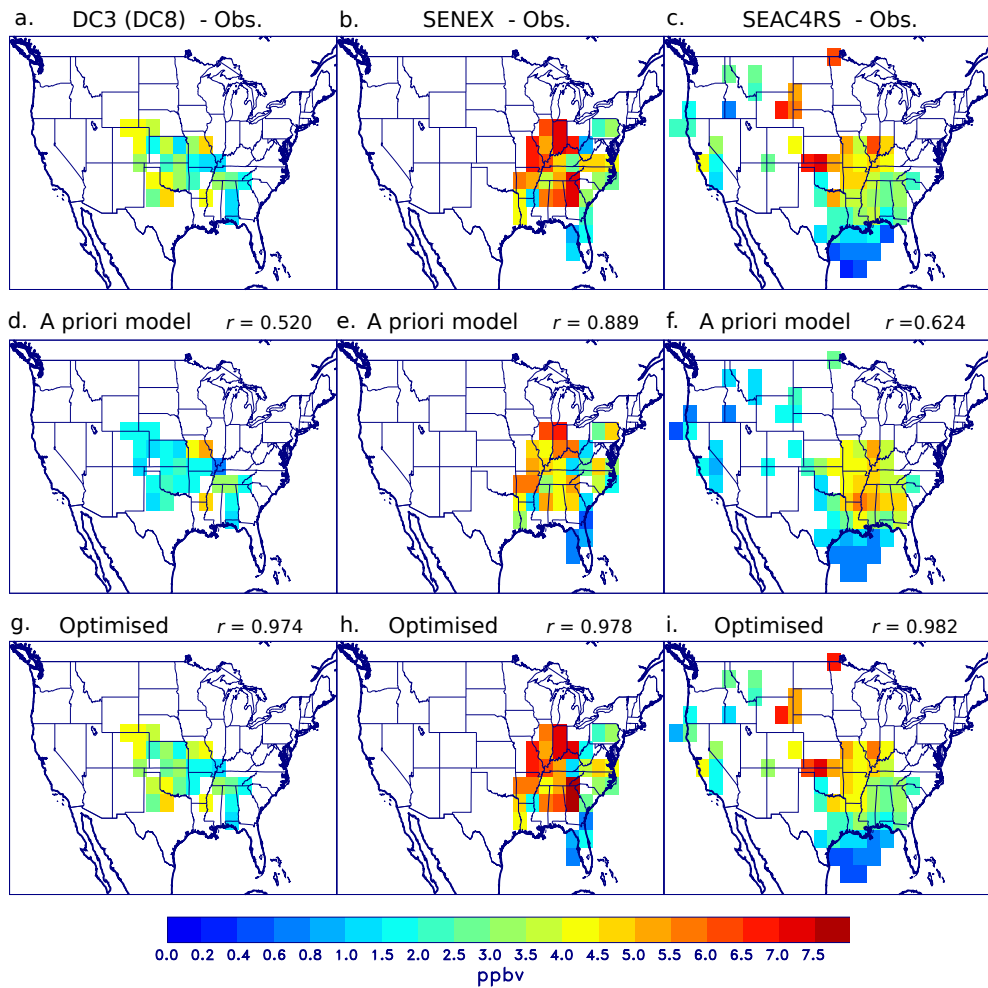


Figure 6. Campaign-averaged distributions of observed CH_3OH concentrations (average below 9 km altitude) from the aircraft campaigns (a) DC3 (DC8), (b) SENEX, and (c) SEAC⁴RS, and corresponding model distributions (d-f) from the a priori model simulation and (g-i) from the aircraft-constrained inversion. Pearson's coefficients of correlation (r) of the modelled with the observed mixing ratios are also given.

420 reaching factors of 2–3 between western Texas and Wyoming (Fig. S3). Small decreases are inferred over large parts of east-
 ern U.S. Since the emission parameters are under-constrained by the inversion due to the poor coverage of the observations,
 the optimised emissions have limited reliability and are strongly dependent on the a priori inventories and inversion setup.
 Nevertheless, the excellent agreement of the optimised model with not only the observational datasets used as constraint in
 the inversion (panels a,c and d in Fig. 7), but also with the TOGA CH_3OH measurements on board the GV aircraft during
 425 the DC3 campaign (panel b in Fig. 7) demonstrates that the optimisation successfully derived a methanol distribution closely
 reproducing the airborne observations.

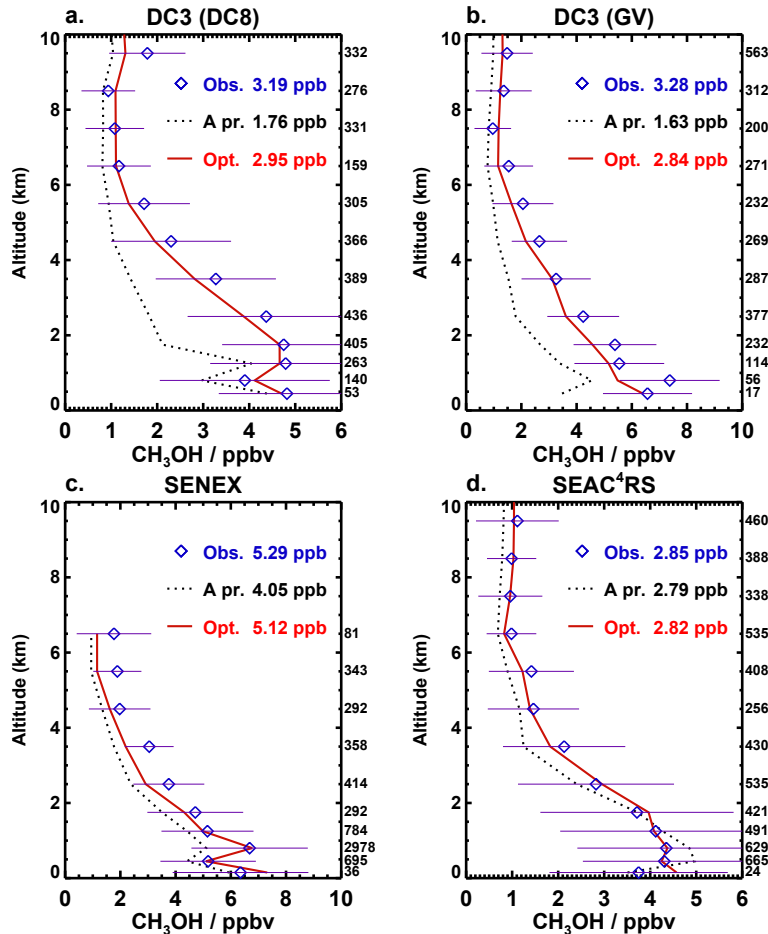


Figure 7. Campaign-averaged vertical profiles of observed CH₃OH concentrations (symbols) from 4 airborne measurement datasets over the U.S.: (a) DC3 (DC8), (b) DC3 (GV), (c) SENEX, and (d) SEAC⁴RS. Dotted lines: corresponding profiles from the a priori model simulation; red lines: aircraft-constrained inversion. The error bars denote the standard deviation of the observations. The number of data per altitude bin is shown on the right of each plot. The average observed and modelled mixing ratios below 8 km altitude are given for each campaign. Data from panel b (DC3 GV) were not used as constraint in the emission optimisation.

The linear regression of the observed and simulated concentrations yields a slope of almost 1 (0.98) and a correlation coefficient of 0.98. However, the comparison of IASI and co-located aircraft-constrained model columns (Fig. 8) shows significant biases. High IASI columns ($> \sim 25 \cdot 10^{15}$ molec. cm⁻²) are underestimated by up to a factor of ~ 1.4 . This underestimation of high columns is consistent across the three campaigns. The statistics of the comparison are improved when the averaging kernels are applied to the model profiles: in particular, the correlation coefficient increases from ~ 0.81 to ~ 0.85 .
 430

An ordinary linear regression of IASI and aircraft-constrained model columns yields

$$\Omega_{\text{IASI}} = 0.46 \Omega_{\text{airc}} + 10.6 \cdot 10^{15}, \quad (17)$$

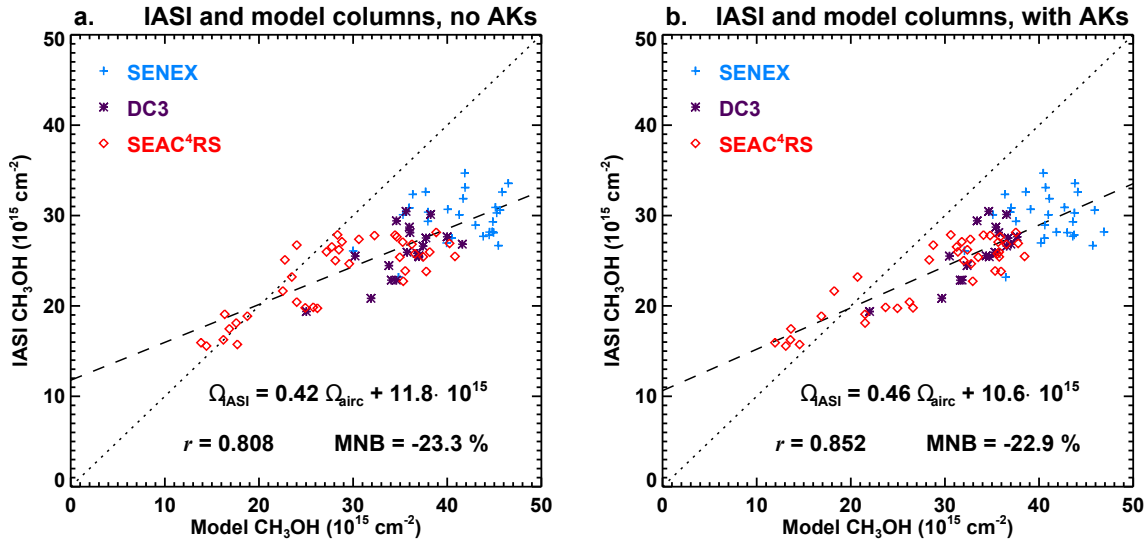


Figure 8. Scatter plots of modelled and observed CH_3OH columns from three aircraft campaigns (SENEX, SEAC⁴RS and DC3 (DC8)). The modelled values are constrained by the aircraft measurements through an emission optimisation as described in the main text. In panel (a), the model columns are calculated without applying the averaging kernels (AKs), whereas in (b), the AKs are applied to the model vertical profiles to compute the columns. Each symbol represents campaign-averaged methanol columns at a model pixel. The correlation coefficients and regression parameters using the Theil-Sen estimator are given in each panel, as well as the median normalized bias (MNB), defined as the median of $(\Omega_{\text{IASI}}/\Omega_{\text{Model}} - 1) \times 100$.

where Ω_{IASI} and Ω_{airc} are the CH_3OH columns (molec. cm^{-2}) from IASI and from the aircraft-constrained model simulation, 435 respectively. The $1-\sigma$ uncertainty is 0.03 for the slope and $1.1 \cdot 10^{15} \text{ molec. cm}^{-2}$ for the intercept. The regression suggests a moderate overestimation of IASI columns in the range $(15 - 20) \cdot 10^{15} \text{ molec. cm}^{-2}$, although the data is too limited to draw firm conclusions. Below that range, the bias remains uncharacterised by the aircraft data used in this study.

The reasons for the IASI biases with respect to aircraft in situ data and for their dependence on the magnitude of the columns are yet unclear. Qualitatively similar biases were derived from the evaluation of OMI and TROPOMI CH_2O columns against 440 aircraft and FTIR data (Vigouroux et al., 2020; Müller et al., 2024). The estimated in situ measurement uncertainties are clearly too low ($\sim 20\%$, see Sect. 2.2) to fully account for the biases derived above, although they could contribute; furthermore, the model biases against the PTR-Q-MS data of the DC3 campaign are validated by the good consistency between the model evaluation against PTR-Q-MS (DC8) and TOGA (GV) measurements from this campaign (Fig. 7a-b). Evaluation against measurements in other regions and using other techniques would be needed to confirm and refine the biases derived in this 445 work.



4 The methanol budget and distribution based on bias-corrected IASI data

Here, we derive top-down methanol emissions based on bias-corrected IASI columns ($\Omega_{\text{IASI,BC}}$) calculated (see Eq. 17) with

$$\Omega_{\text{IASI,BC}} = (\Omega_{\text{IASI}} - 10.6 \cdot 10^{15}) / 0.46. \quad (18)$$

Figure 9 displays the seasonally averaged CH_3OH columns from IASI (bias-corrected), the a priori model simulation and 450 the IASI-based emission optimisation. The seasonal cycle of the columns over large regions is shown on Fig. S4. The a priori model succeeds in reproducing the general features of the satellite observations, such as high columns ($\sim 40 - 90 \cdot 10^{15} \text{ molec.cm}^{-2} \text{ s}^{-1}$) throughout the year over tropical continents, and a pronounced summertime peak at extratropical latitudes, consistent with previous spaceborne methanol distributions (Stavrakou et al., 2011; Cady-Pereira et al., 2012; Wells et al., 2025). Both the a priori model and the IASI data display a substantial longitudinal gradient of methanol columns over 455 northern Eurasia during summer, with low values over western Europe and a broad maximum over eastern Siberia. There are also important differences between IASI and the a priori model, most notably a large model underestimation at extratropical northern latitudes during all seasons, reaching a factor of about 2 over Central Asia, Siberia and Canada during summer, and an overestimation of the columns over Amazonia near the end of the wet season (May–July, see Fig. S4). Furthermore, although the a priori model columns peak at the same month as the satellite data at mid-latitudes (most often July), the model underestimations are more pronounced during spring and early summer (i.e. May–July) than in the following months (August–October), 460 in particular over the U.S., China and Europe (Fig. S4).

The emission optimisation successfully closes the gap between the model and the observations, in particular over tropical regions and at extratropical latitudes during summer (Fig. 9 and Fig. S4). During winter at high northern latitudes, however, the large a priori model underestimation remains unchanged after optimisation. This is explained by the weakness of methanol 465 emissions and by the low number of IASI measurements used in the optimisation at these latitudes during winter, compared to other latitudes and seasons (Fig. S5). Similar results were obtained by Wells et al. (2014) in their emission optimisation based on CH_3OH column data from TES. Interestingly, although the focus of our study is on continental areas, the agreement of MAGRITTE methanol columns with IASI is also substantially improved over oceanic areas (panels p-s on Fig. S4) after inversion, especially at extratropical latitudes (except in winter).

470 This improved agreement with IASI data is primarily achieved through changes in the distribution of biogenic methanol emissions (Fig. 10). The biogenic emissions are strongly enhanced over North America and most of Eurasia after inversion, while biogenic emissions due to tropical forests are generally decreased, in particular over Amazonia and Indonesia, and emissions due to tropical savanna over Africa, Australia and eastern Brazil are increased (Fig. 3). As in previous inversion studies (Stavrakou et al., 2011; Wells et al., 2014), the strongest enhancements (up to a factor 5) are derived over arid and semi-arid landscapes such as Central Asia, Western U.S. and the Sahel region (Fig. 10-11). This underestimation might partly result 475 from the neglect of soil emissions in MEGAN. Soils (including litter decomposition) are indeed a known methanol source (Warneke et al., 1999), and although their contribution is generally considered to be small, typically 1–2 orders of magnitude lower than foliage emissions (Peñuelas et al., 2014), they might be more significant over sparsely vegetated areas characterised by low LAI.

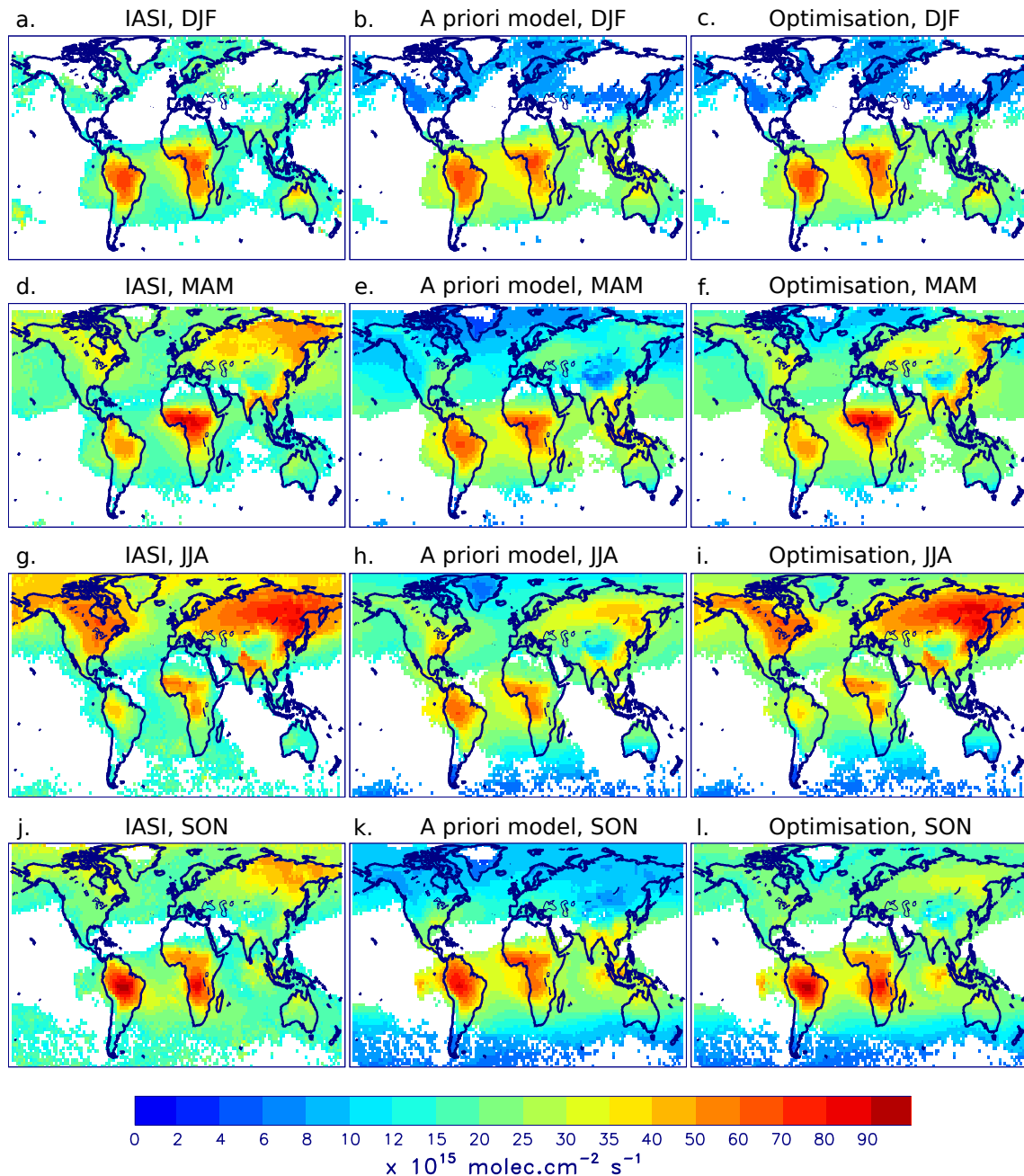


Figure 9. 2008–2019 average of CH₃OH columns (10^{15} molec.cm⁻²) from (a) IASI (bias-corrected as described in the text), (b) the a priori model and (c) the model with optimised emissions, for December–January–February. Panels (d–f), (g–i) and (j–l) are as (a–c) but for March–April–May, June–July–August and September–October–November, respectively.

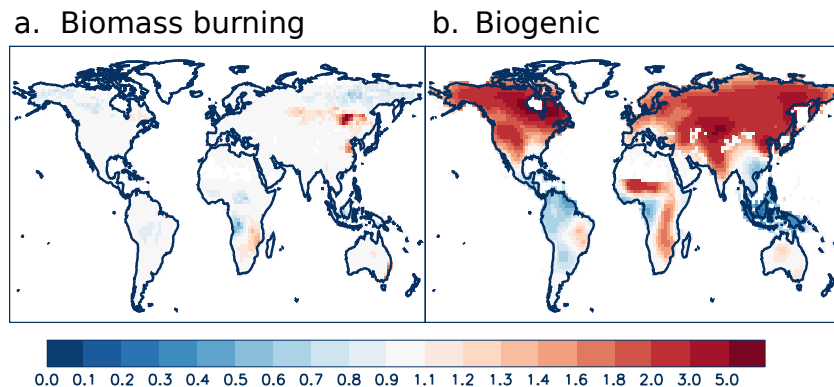


Figure 10. Ratio of top-down to a priori emissions (2008–2019 averages) for (a) pyrogenic and (b) biogenic CH_3OH emissions.

480 The biogenic emission enhancement at mid-latitudes is highest in spring (Fig. S6), and especially in May (Fig. 11). The
underestimation of springtime emissions was previously noted by e.g. Wells et al. (2012). The resulting top-down biogenic
emissions peak earlier than in the MEGAN inventory, in particular over Europe, Eastern U.S., China and Central Asia. Boreal
regions do not follow this trend, with emission enhancements of similar magnitudes being derived over spring, summer and
fall over these regions (Fig. S6). However, the large emission increase during fall (and to a lesser extent during summer)
485 inferred over boreal forests is partly explained by the strong deposition sink (Fig. S2). Since the deposition velocities might be
overestimated over boreal forests (Sect. 2.5.5), the top-down emissions might be also too high, especially during fall. In fact,
in spite of the large emission enhancement derived over Siberia, the net emission flux over this region (Fig. 11) is lower than
the a priori (MEGAN) gross flux.

490 The seasonal cycle of terrestrial emissions undergoes important changes after optimisation over tropical ecosystems (Fig. 11).
Over both northern Hemisphere (NH) Africa and southern Hemisphere (SH) Africa, the biogenic emissions are decreased (by
~25%) at the start of the biomass burning season (November–December in NH, June–July in SH), while these emissions are
strongly enhanced (by up to 70–100%) in the following months (February–June in NH, August–January in SH), until after the
end of the burning season. The optimisation also shifts by one month the seasonal peak of pyrogenic emission over SH Africa
495 (from July in the a priori to August in the optimisation, see Fig. 11), although, as explained above (Sect. 2.7), the dominance of
the biogenic flux makes the top-down results uncertain for biomass burning emissions.

500 The top-down biogenic emissions over tropical ecosystems are strongly correlated with temperature and especially solar
radiation. Over each of the 5 tropical regions shown on Fig. 11 (panels f–g), the two least-emitting months according to the
inversion are the months with the lowest visible radiation fluxes, based on the ERA5 reanalysis. For example, over Amazonia,
the lowest monthly biogenic fluxes (0.54 and $0.61 \text{ Tg month}^{-1}$, about a factor of two below the annual average) are derived
in May and June, which are the months with the lowest visible radiation fluxes ($\sim 85 \text{ W m}^{-2}$, 12% below the annual average).
The same holds for S.-E. Asia and NH Africa (panels f–g), for which the minimum occurs in November–December, and
for Equatorial and Southern Africa (h–i), which have their minimum in June–July. At all 5 tropical regions, the top-down

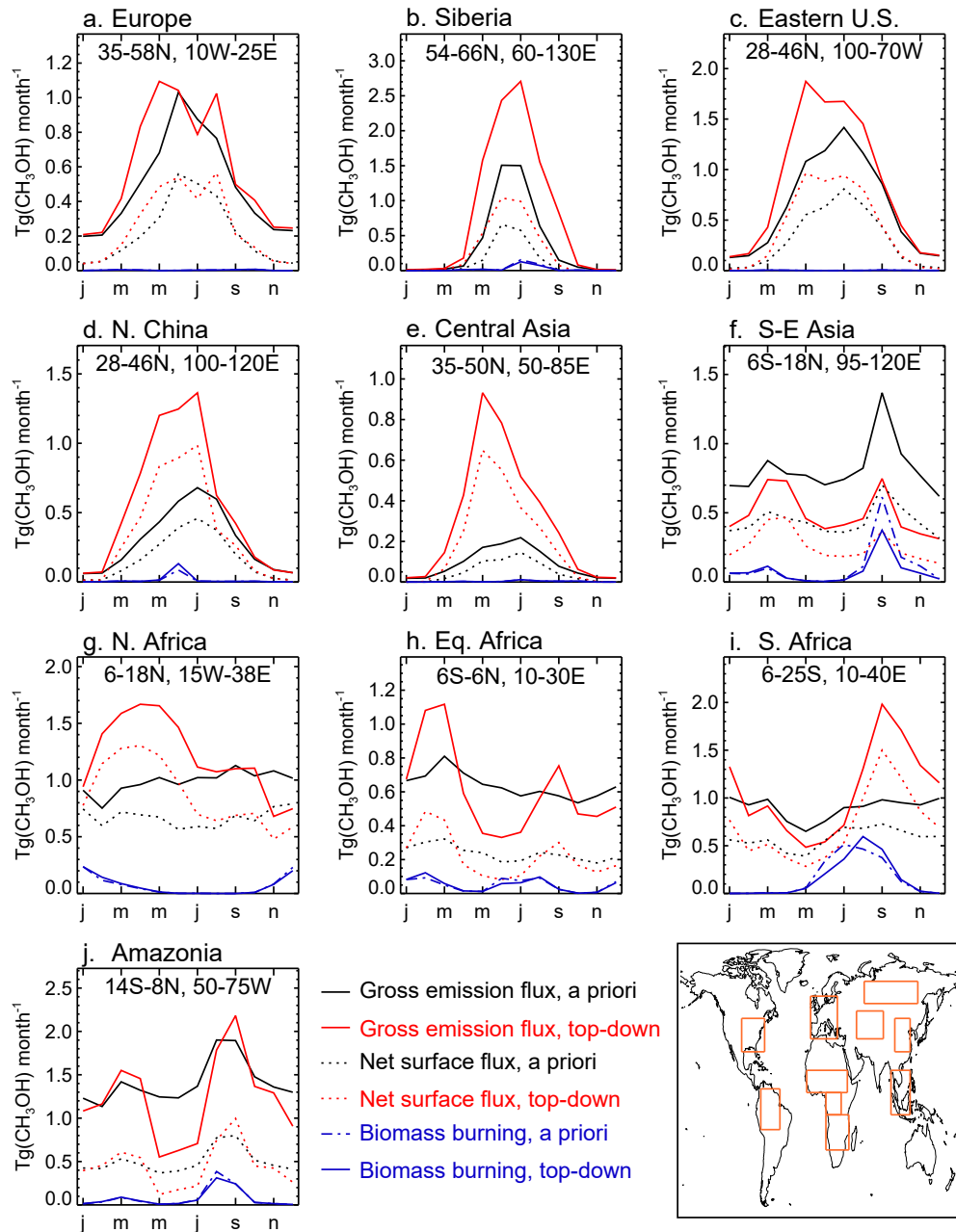


Figure 11. Seasonal cycle of emissions (Tg month⁻¹) over large regions (2008–2019 averages). Black and red solid lines: gross total emission fluxes from the a priori and optimised runs (sum of biogenic, pyrogenic, oceanic and anthropogenic contributions); black and red dotted lines: net emission fluxes, i.e. dry deposition (including ocean uptake) is subtracted from the gross fluxes; dash-dotted and solid blue lines: a priori and top-down biomass burning fluxes.



monthly biogenic emissions correlate strongly with solar visible radiation fluxes, with Pearson's correlation coefficients ranging between 0.79 (Amazonia) and 0.94 (SH Africa). A strong correlation is also found between biogenic emissions and near-surface 505 temperature over NH Africa (0.92) and SH Africa (0.84). At the other regions (panels h-j), the temperature variations are weak (standard deviation of $\sim 0.6\text{K}$) and therefore likely less relevant for biogenic emission variability.

Radiation fluxes and temperature appear to exert a stronger control on biogenic emissions of methanol than is currently accounted for in MEGAN. This control is likely indirect, i.e. phenological changes associated with the seasonal cycle of meteorological variables likely cause variations in the emissions that are currently not represented in the model parametrisations. 510 Over Amazonia, leaf flushing during the wet-to-dry transition period has been suggested to explain a strong reduction of isoprene emissions around May every year (Barkley et al., 2009), and was also proposed to decrease methanol emissions in July (Wells et al., 2025). The growth of new leaves after the wet-to-dry transition period might cause an enhancement of methanol emissions, since young leaves are known to emit at higher rates than mature leaves. However, the MODIS LAI dataset indicates only a moderate and progressive increase of LAI during this period, from ~ 4.2 to $\sim 5.2 \text{ m}^2 \text{ m}^{-2}$ between February and 515 September. Since the parametrisation of the leaf age response factor in MEGAN (γ_{age}) relies on the temporal variation of LAI between time steps, the proportion of new or growing leaves calculated in this way is very small, and γ_{age} is close to unity. More work is needed to understand the impact of phenological changes on methanol emissions, and how these changes can be represented in emission models.

The global top-down biogenic emission flux is 160 Tg yr^{-1} , i.e. 23% higher than our a priori from MEGAN (130 Tg yr^{-1}), 520 and almost 60% higher than previous top-down estimates based on in situ data (Millet et al., 2008; Bates et al., 2021) or spaceborne IASI columns (Stavrakou et al., 2011) (Table 2). The total terrestrial emissions, amounting to 178 Tg yr^{-1} globally, are also 46% higher than the top-down best estimate of 122 Tg yr^{-1} based on TES column retrievals (Wells et al., 2014). The optimisation leads to very small changes in the anthropogenic and pyrogenic emission categories, not exceeding a few percent at the global scale (Table 2).

525 Despite the large enhancement of methanol emissions inferred in this study, the global atmospheric burden of methanol, 3.4 Tg in our optimisation, is only slightly higher (by 9–17%) than in previous modelling studies constrained by observations (Table 2). The larger methanol loading (by 17%) compared to the IASI-based inversion by Stavrakou et al. (2011) is largely due to the bias correction of IASI data (Eq. 18), leading to column increases of the order of 30% over source regions (Sect. 3). The main reason for the larger enhancement of terrestrial emissions, compared to previous inversion studies, is the sink due 530 to dry deposition over land, 72 Tg yr^{-1} globally, about a factor of 2.6 larger than in the inversion studies of Stavrakou et al. (2011) and Wells et al. (2014), but very close to a global sink estimate based on in situ CH_3OH measurements and a dry deposition velocity of 0.4 cm s^{-1} (70 Tg yr^{-1} , Heikes et al., 2002). The global lifetime of atmospheric methanol with respect to dry deposition over land is ~ 17 days, well below the range of reported values, 26–38 days (Jacob et al., 2005; Millet et al., 2008; Stavrakou et al., 2011; Bates et al., 2021). Due to this strong sink, the net terrestrial source of methanol inferred here is 535 only slightly (+10%) larger than in the inversion studies of Stavrakou et al. (2011) and Wells et al. (2014). As seen on Fig. 11, the gross top-down emission fluxes over forested regions such as Amazonia, Equatorial Africa and Siberia (14.7 , 7.3 and 9.4 Tg yr^{-1} , respectively) are up to a factor of 3 higher than the net surface fluxes accounting for dry deposition (5.4 , 2.6 and



Table 2. Global methanol budget ($\text{Tg}(\text{CH}_3\text{OH}) \text{ yr}^{-1}$) averaged over 2008–2019 in the a priori simulation and after optimisation of emissions based on bias-corrected IASI data, and comparison with previous budget studies constrained by atmospheric observations. Notes: ^a: Sum of biogenic, anthropogenic and biomass burning sources in Wells et al. (2014). ^b: The oceanic source and atmospheric photochemical production are not optimised in this study.

	Millet et al. (2008)	Stavrakou et al. (2011)	Wells et al. (2014)	Bates et al. (2021)	This study (a priori)	This study (optimisation)
<i>Sources</i>						
Total source	242	187	225	205	243	271
Biogenic	103	100		101	131	160
Anthropogenic	5	9.3	122 ^a	6.3	10.5	10.6
Biomass burning	12	4.3		13	7.8	7.5
Oceanic	85	43	66	24	47	47 ^b
Secondary production	37	31	37	60	46	46 ^b
<i>Sinks</i>						
Atmospheric oxidation	88	108	70	116	119	132
Ocean uptake	101	48	73	38	59	61
Wet deposition	13	3	9.5	11	6.3	6.5
Dry deposition to land	40	28	26	41	59	72
Burden (Tg)	3.1	2.9		3.0	3.1	3.4
Lifetime (days)	4.7	5.7		5.3	4.7	4.5

3.2 Tg yr^{-1}). Over less productive ecosystems, including regions with large biomass burning fluxes, the gross and net fluxes are more similar, but still significantly different, e.g. by factors of 1.4–1.6 for Central Asia, North Africa and South Africa. At 540 global scale, dry deposition over land offsets about 45% of the biogenic emission flux (Table 2).

The deposition velocities computed in this work, typically between 0.2 and 1.6 cm s^{-1} over vegetated areas (Fig. S2) are well-supported by measurement-based estimates (Fig. 4), except for a large overestimation at a boreal forest site (Hyytiälä) (Sect. 2.5.5). The large dry deposition sink inferred by the model over boreal forests is therefore likely overestimated, and the biogenic emission enhancement at high latitudes (Fig. 10) might also be too high. Elsewhere, however, the strong dry deposition sink is consistent with available data. Over the tropical forests of Amazonia, Central Africa, Indonesia and southeast Asia, and 545 even over Europe and eastern U.S., dry deposition is found to be a stronger sink of methanol than chemical oxidation due to reaction with OH (Fig. 3).

The optimised methanol budget presented in Table 2 bears uncertainties due to potential errors in the IASI data used as 550 constraints and because, while terrestrial emissions are optimised, the other productions and the sinks of methanol have their own uncertainties. In particular, oceanic emissions depend on assumed seawater methanol concentrations for which available field campaign data show a very strong variability (Bates et al., 2021). Replacing the seawater concentration adopted in the



model (Sect. 2.5.4) by the value of 61 nmol l^{-1} determined by Bates et al. (2021) based on an analysis of ATom data would decrease the oceanic emission flux from 47 Tg yr^{-1} globally to 24 Tg yr^{-1} , in excellent agreement with Bates et al. (2021). The photochemical production of methanol due to the $\text{CH}_3\text{O}_2 + \text{OH}$ reaction is also uncertain; for example, adoption of a 555 fixed methanol yield of 13% from the reaction (Bates et al., 2021), in place of the current model assumptions (Sect. 2.5.2), would increase the global CH_3OH production by $\sim 5 \text{ Tg yr}^{-1}$. However, the impact of these uncertainties on the optimisation of continental emissions is very small. A sensitivity inversion performed for one year (2017) for which the marine source and the methanol yield from $\text{CH}_3\text{O}_2 + \text{OH}$ both follow the recommendations of Bates et al. (2021) leads to negligible impacts on 560 top-down terrestrial emissions (+1.1% compared to the standard inversion) and on dry deposition fluxes over land (+0.4%), in spite of more sizeable impacts on the global CH_3OH burden (-4.9% , to 3.25 Tg yr^{-1}) and on global oceanic uptake (-19% , to 4.9 Tg yr^{-1}).

5 Model evaluation against in situ and ground-based remote sensing data

5.1 Evaluation against in situ airborne data

The emission optimisations being constrained by IASI columns that are bias-corrected using aircraft data (Sect. 3), the model 565 evaluation against aircraft observations is expected to improve after optimisation. Figure 12 and Table S4 show that this is indeed the case: on average for all campaigns over land (weighted by the number of data below 8 km altitude), the bias is decreased from -23% in the a priori simulation to -8% after optimisation, and the root-mean-square-deviation (RMSD) is also decreased (Table S4). The comparison statistics are improved for all but one campaign (ARCTAS-July, see further below). Over oceans as well, the optimisation of terrestrial emissions improves the model agreement with in situ measurements from 570 the ATom campaigns (Fig. 2), especially at northern latitudes ($> 25^\circ$, see Fig. S7). The comparisons with GoAmazon and SEAC⁴RS measurements support the biogenic emissions decrease over Amazonia as well as over southeastern U.S. in late summer/early fall (Fig. S6), while the comparisons against the DC3, SENEX, ARCTAS-June and KORUS-AQ campaigns support the springtime enhancement of methanol emissions over terrestrial ecosystems at mid-latitudes (Fig. 11 and Fig. S6).

The improved model agreement against KORUS-AQ is realized through substantial increases of biogenic emissions, by 575 factors of up to 3 over Korea and up to 6 over northeastern China. The a priori anthropogenic emissions being very weak (Fig. 3), these emissions are essentially unchanged by the inversion (+15% increase over Beijing). Beaudry et al. (2025) showed that elevated methanol and ethanol near-surface concentrations in urban areas of South Korea and China are likely largely due to anthropogenic Volatile Chemical Products (VCPs) from the residential sector, currently missing in global emission inventories. Beaudry et al. (2025) estimated the anthropogenic CH_3OH emissions from China alone to be 9.3 Tg yr^{-1} in 2016, two orders 580 of magnitude above the inventory estimate used in MAGRITTE. VCP-related methanol emissions are much lower in the U.S. due to regulations of their usage as a result of their toxicity. Part of the methanol emission increase inferred by our inversion might therefore be wrongly attributed to biogenic emissions. In the free troposphere during KORUS-AQ, the strong correlation of methanol with acetone suggested an important biogenic contribution, however. Furthermore, the seasonal variation of top-down methanol emissions over northern China (Fig. 11d) shows a much stronger enhancement in spring than in fall, similar

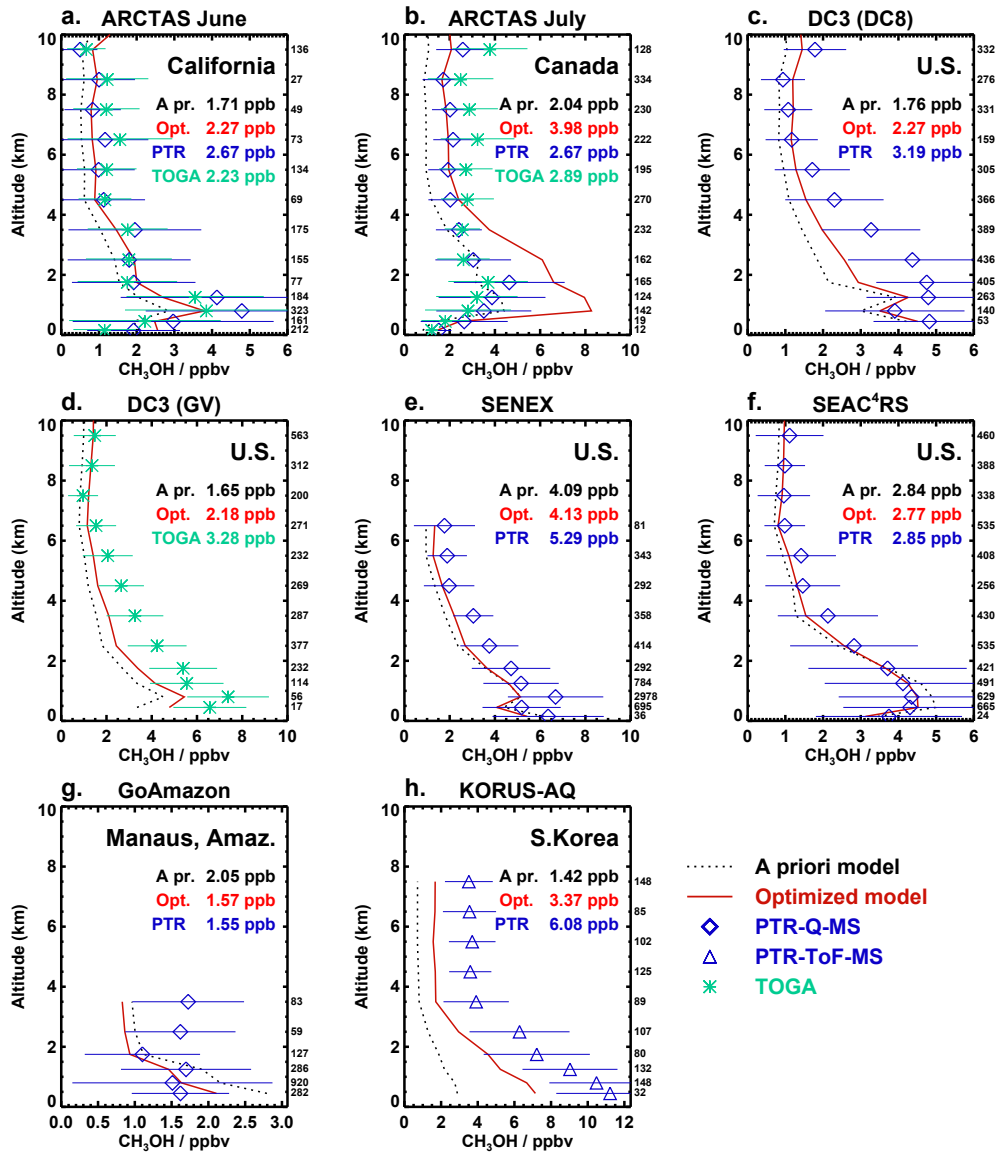


Figure 12. Averaged vertical profiles of observed CH_3OH concentrations (symbols) from aircraft campaigns: (a) ARCTAS June, (b) ARCTAS July, (c) DC3 (DC8), (d) DC3 (GV), (e) SENEX, (f) SEAC⁴RS, (g) GoAmazon, and (h) KORUS. Dotted lines: corresponding profiles from the prior model simulation; red lines: IASI-based optimisation. The error bars denote the standard deviation of the observations. The number of measurements per altitude bin is indicated on the right of each plot. The average observed and modelled mixing ratios below 8 km altitude are given for each campaign. Data over ocean are excluded from all averages. Only measurements over Canada ($> 49^\circ$) are retained in the ARCTAS-July profile.



585 to other regions at mid-latitudes and consistent with a predominantly biogenic source. Incorporation of VCP emissions in methanol emission inventories will be needed to improve the assessment of biogenic emissions over East Asia.

In contrast with all other campaigns, for which the model performance improves after optimisation (Table S4), the model agreement with respect to the July ARCTAS dataset deteriorates when optimised emissions are used. The emission increase inferred by the inversion reaches a factor of ~ 3 in the region, due to the high (bias-corrected) IASI columns ($\sim 5 \cdot 10^{16}$ molec. cm^{-2})
590 typical of Central Canada during summer (Fig. 9). This leads to overestimated concentrations below 4 km altitude in comparison with both TOGA and PTR-MS measurements (Fig. 12b). Important fire events took place in this area during this campaign, and the CH_3CN -based criterion used to filter out pyrogenic influences removed $\sim 26\%$ of the data, while also reducing the average observed mixing ratio by 21%. A test evaluation without this filter (not shown) leads however to similar conclusions. The model overestimation for the entire methanol column below 10 km, calculated from the vertical profiles shown on Fig. 12b,
595 amounts to a factor of ~ 1.4 . This factor is similar to the enhancement of the IASI column due to the bias correction (factor of ~ 1.5 , see Eq. 18). Therefore, an emission optimisation constrained by uncorrected IASI columns would likely lead to a closer agreement with the ARCTAS-July campaign, although it would worsen the comparison with all other campaigns. The reason for the singularity of ARCTAS-July is unknown.

5.2 Evaluation against in situ surface data

600 The emission optimisation also significantly improves the model comparison with surface concentrations data, as seen on Fig. 13 (also Fig. S1). The Pearson's correlation coefficient is increased from 0.66 to 0.89 after emission inversion, and the median bias becomes very small. As detailed in Table S5, the large positive bias of the a priori run at the sites located in tropical forests (+56% on average for 10 measurement campaigns) is strongly reduced, to 15% after optimisation, providing additional support to the emission decrease inferred over tropical forests. Over Europe, U.S.A., East Asia and marine sites as well, the
605 biases are generally reduced, from respectively -16%, -17%, -44% and -17% in the a priori simulations, to -1%, +17%, -19% and -7% with optimised emissions.

A further illustration of the model performance against in situ data over temperate ecosystems is provided by the comparison of modelled methanol against PTR-MS measurements at Vielsalm and Lonzée in 2009–2013 (Fig. 14). At both sites, only a small bias remains after emission optimisation (7% at Vielsalm and -14% at Lonzée), and the model generally succeeds in
610 reproducing the shape of the seasonal cycle (overall Pearson correlation r of 0.84).

5.3 Evaluation against FTIR column data

Figure 15 displays the observed and modelled average seasonal cycle of methanol columns at the 8 FTIR stations, whereas Fig. S8 shows the full time series of monthly columns and Table S6 provides the summary of comparison statistics. The averaging kernels and sampling times of the measurements are accounted for in the calculation of model columns. At Porto Velho, the
615 standard optimisation leads to an unrealistic large peak in September 2019 (Fig. 15f) due to the monthly resolution of emission increments and to a large temporal variability of methanol columns in the course of the month. The FTIR measurements for September having been all recorded during the first 12 days of the month, an additional emission inversion was performed for

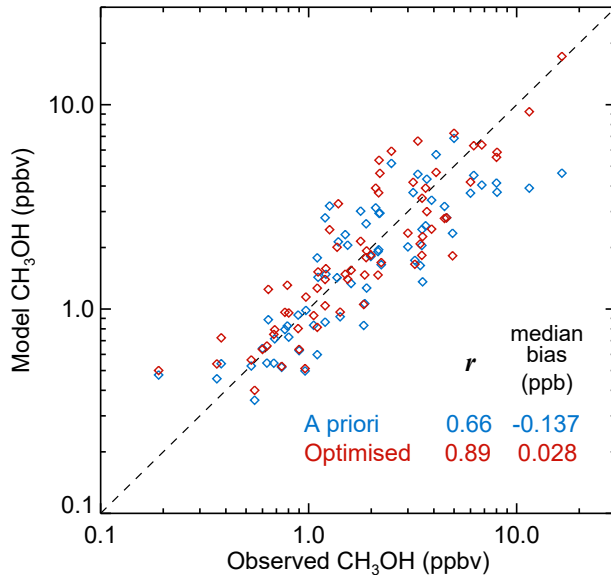


Figure 13. Scatter plots of averaged modelled and observed in situ CH_3OH mixing ratios at the sites listed in Table S1. Blue: model results using a priori emissions; red: IASI-based simulations. Pearson's correlation coefficient (*r*) and the median bias over all sites are also given.

year 2019, identical to the standard run except that IASI data between 13 and 30 September were excluded. The result of this inversion (dotted red line on Fig. 15f) differs from the standard run only in September, and leads to a much improved seasonal 620 cycle against FTIR data.

At all sites except St Petersburg, the optimisation reduces the model biases and RMSD (Table S6). Furthermore, the optimised model correlates very well with the data at all sites, with Pearson's correlation coefficients ranging from 0.78 (Eureka) to ~ 0.95 (Porto Velho and Kitt Peak). At the three mid-latitudes sites (Toronto, Jungfraujoch and Kitt Peak), the negative biases of the a priori run with respect to the data (between 20 and 30%) are replaced by moderate biases ($\pm 12\%$ or better) and the 625 improved seasonal cycle at Kitt Peak supports the large emission enhancement in spring and early summer at these latitudes. The low biases at Kitt Peak and Jungfraujoch contrast with the evaluation of a previous inverse modelling study constrained by IASI data at these sites (Stavrakou et al., 2011; Bader et al., 2014). At both stations, the optimised model underestimated the summertime FTIR columns by up to a factor of 1.5. The probable reasons for the improvement are multiple, including the IASI retrieval updates, the bias-correction of IASI columns, and the higher spatial resolution and longer time series considered 630 in this work.

At St Petersburg, the optimised model overestimate the data (+21%), especially during summer when the columns are high. The overestimation reaches a factor of 1.44 during May–August, when the bias correction of IASI columns (Eq. 18, for IASI 635 columns of $\sim 30 \cdot 10^{15} \text{ molec. cm}^{-2}$) enhances the columns by a factor ~ 1.41 . Therefore, as for the model comparison with in situ measurements of the ARCTAS-July campaign (Sect. 5.1), an optimisation constrained by uncorrected IASI columns would have yielded a better agreement with the FTIR observations than the optimisation presented above. The similar conclusions

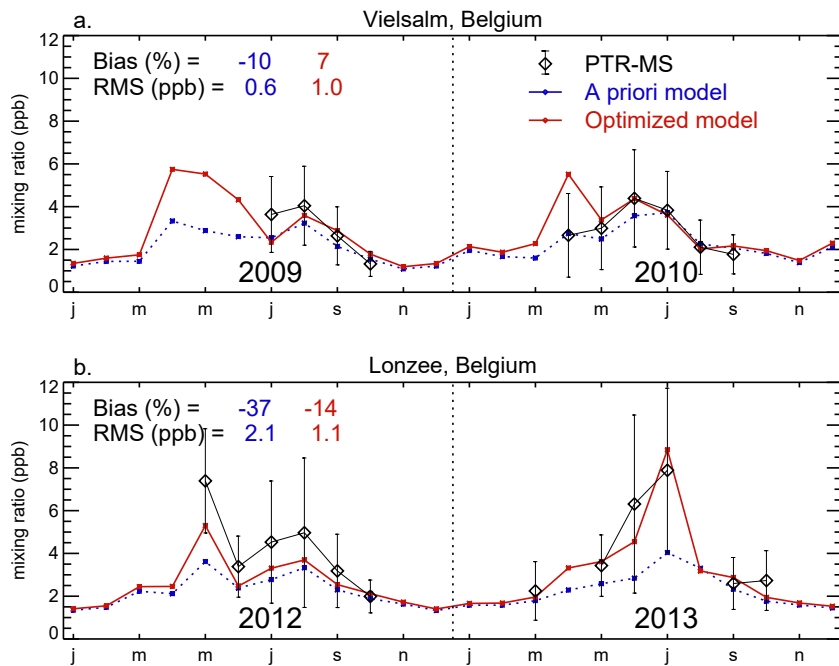


Figure 14. Time series of monthly-averaged observed CH_3OH concentrations (symbols) and corresponding model results from the a priori run (dotted) and from the IASI-based optimisation (red) at (a) Vielsalm (50.305°N , 5.999°E) in 2009–2010 and (b) Lonzée (50.552°N , 4.745°E) in 2012–2013. The relative bias and root-mean squared deviation (RMS) are given for each site. The error bars denote the standard deviation of the monthly averaged data.

drawn from FTIR and airborne campaign data obtained in similar environments, namely the vast area of high columns within the boreal land masses at around 60°N during summer (Fig. 9), strongly suggest that the bias correction derived from airborne data in Sect. 3 is inappropriate in such environments.

Large model biases are also found at Porto Velho (24% for the 5-month average), especially in September (39%) and October 640 (59%). However, when taking into account the number of FTIR data recorded per month, lowest in September–October (46 and 7, respectively) and highest in July (286), the relative bias amounts to only 13%, down from 37% in the a priori simulation. This small remaining bias is consistent with the model evaluation against surface in situ data in tropical ecosystems (+15% bias, Sect 5.2) and the GoAmazon campaign (negligible bias, Sect. 5.1). The comparisons at the two Reunion island stations (St Denis and Maïdo) show also small positive biases (4–11%).

645 6 Conclusions

Twelve years of IASIv4 global methanol column data are used in an inverse modelling framework built on the MAGRITTEv1.2 model to propose an updated assessment of CH_3OH global distribution and terrestrial emissions. The IASIv4 dataset is gener-

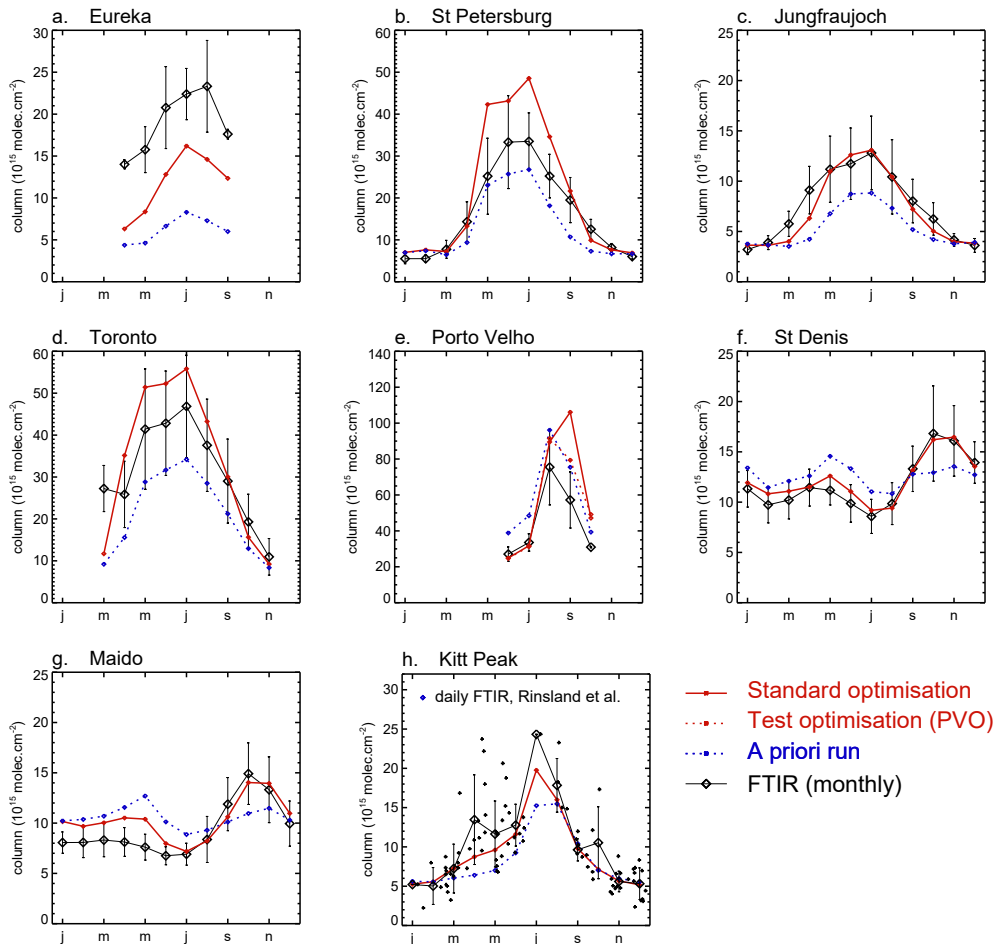


Figure 15. Monthly CH_3OH FTIR columns (10^{15} molec. cm^{-2}) averaged over 2008–2019 (black lines and diamonds) and corresponding averages from the a priori simulation (dotted blue) and optimised model (red) at (a) Eureka, (b) St Petersburg, (c) Jungfraujoch, (d) Toronto, (e) Porto Velho, (f) St Denis, and (g), Maido. The FTIR averaging kernels and sampling times are accounted for in the calculation of the model columns. The dotted red line in panel (e) denotes model columns from a test optimisation in which IASI data between 13 and 30 September 2019 were excluded. Panel (h) displays the average seasonal cycle of FTIR columns (2.09–14 km above sea level) recorded at Kitt Peak between 1985 and 2003 (Rinsland et al., 2009), compared with the 2008–2019 climatological average from the model. The daily FTIR averages (Fig. 5 of Rinsland et al., 2009) are also shown. The error bars denote the standard deviations of the monthly data.

ated using the ANNI version 4 retrieval framework, which incorporates several methodological advances compared to previous versions. In particular, the dataset includes total-column averaging kernels, essential to minimise the impact of vertical-profile differences in the comparisons between IASI retrievals and MAGRITTE outputs.

In a first step, in situ methanol observations from three extensive aircraft campaigns over the U.S. (DC3, SENEX and SEAC⁴RS) are assimilated into the model to derive aircraft-constrained model distributions used to evaluate the IASI columns.



The results suggest an underestimation of large IASI columns, reaching a factor of 1.41 for IASI columns of $\sim 30 \cdot 10^{15}$ molec. cm $^{-2}$. The in situ measurement uncertainties are too low to account for these biases, which therefore remain unexplained.

The bias of IASI with respect to aircraft data is tentatively corrected through a linear relationship, and the bias-corrected IASI columns are used as constraints to optimise the terrestrial CH₃OH emissions in the MAGRITTE global model over 2008–2019. Model evaluation against nine aircraft datasets spanning 2008–2018 shows that the emission optimisation leads to a large reduction of the average bias against aircraft observations over land, from -23% in the prior simulation to -8.4% in the optimisation; the model agreement is also improved over oceans. Similarly, the model performance against a broad compilation of surface in situ data (67 campaigns) is greatly improved, as seen from the resulting high correlation and low biases globally and regionally (less than 20% bias over tropical forests, U.S., Europe, East Asia and marine areas). The model performance (bias and RMSD) is also improved at seven of the eight FTIR stations.

Nevertheless, closer examination of the comparisons points to important regional differences. Most noticeably, the optimisation leads to substantial model overestimations (by 40%) against summertime measurements over the Canadian boreal forest (ARCTAS-July campaign) and in northern European Russia (St Petersburg), suggesting that the bias correction of IASI columns is unwarranted at these latitudes. Over tropical ecosystems, the comparisons with in situ data (10 campaigns) and FTIR data (at Porto Velho and Reunion island) suggests a small positive bias ($\sim 15\%$), despite a substantial reduction of biases, in comparison to the prior simulation. Future work should aim at a better characterisation of IASI biases using aircraft and surface in situ data (especially over boreal and tropical ecosystems, poorly represented in the present study) and FTIR data (in all environments), considering the small number of stations where methanol is being retrieved.

The emission inversion suggests largely increased biogenic emissions over North America and most of Eurasia as well as decreased emissions over tropical forests. Strong enhancements, by up to a factor 5, are found over semi-arid ecosystems, consistent with previous inversion studies and possibly due to soil emissions currently overlooked in MEGAN. The seasonal cycle of biogenic emissions undergoes significant changes. At mid-latitudes, the optimised emissions peak earlier than in the MEGAN inventory. Over tropical ecosystems, emission increases are inferred during warm and sunny periods, while decreases are derived during colder, less sunny months. Temperature and visible radiation fluxes appear to exert a stronger control of biogenic emissions than can be accounted for in MEGAN, for reasons still unclear. A revision of the parametrisation of the leaf age response factor is likely needed for tropical environments.

The global top-down biogenic emission flux (160 Tg yr^{-1}) is almost 60% higher than previous top-down estimates (Millet et al., 2008; Stavrakou et al., 2011; Bates et al., 2021), due to mainly two reasons. The first reason is the bias correction of IASI columns, corroborated by the improved model performance against a wide range of observations, except over boreal continental regions, as noted above. The total biogenic flux due to boreal forests is increased by a factor of 2.4, from 9.4 to 22.8 Tg yr^{-1} . Even without the contribution of boreal forests, the global top-down biogenic flux would therefore still be much higher than previous estimates. The second reason is the stronger sink due to dry deposition in our model, with a global lifetime with respect to this process of 17 days, well below the range of estimates from previous modelling studies. Dry deposition is estimated here to offset 45% of the global biogenic emission flux. The deposition velocities are calculated using a Wesely-type



parametrisation adjusted based on estimates from 13 field campaign studies. The calculated values range typically between 0.2 and 1.6 cm s⁻¹ over vegetated areas, in generally good agreement with the field studies. A notable exception is the boreal forest site of Hytylä, where the deposition velocity is largely overestimated. Therefore, the dry deposition sink (and also the top-down biogenic gross flux) might be similarly overestimated over these forests. Clearly, more field campaign data are needed to provide a better assessment of both methanol abundances and dry deposition velocities in this environment, and more generally over terrestrial ecosystems.

Data availability. The NASA aircraft campaign datasets are available from the Langley Research Center at <https://www-air.larc.nasa.gov/missions/merges> (last access: 16 January 2026). The Vielsalm dataset for 2009 and 2010 is available at <https://doi.org/10.18758/h659pdvr> (Amelynck et al., 2024a), while the Lonzée dataset is available at <https://doi.org/10.18758/7v20vh47> (for 2012) (Amelynck et al., 2024b) and <https://doi.org/10.18758/7v20vh47> (for 2013) (Amelynck et al., 2024c). The MEGAN-MOHYCAN methanol emissions and the top-down methanol emissions generated in this study are available at <https://emissions.aeronomie.be> (Müller et al., 2026). The monthly LAI distributions from MODIS15A2H collection 6 are available at <https://lpdaac.usgs.gov> (last access: 15 January 2026).

700 Appendix A: Details on the dry deposition scheme

A1 Aerodynamic resistance

The aerodynamic resistance (s m⁻¹) is expressed (ECMWF, 2021) as

$$R_a = \frac{1}{\kappa u_*} \left[\ln\left(\frac{z_l + z_{0M}}{z_{0H}}\right) - \Psi_H\left(\frac{z_l + z_{0M}}{L}\right) + \Psi_H\left(\frac{z_{0H}}{L}\right) \right] \quad (\text{A1})$$

with κ von Karman's constant (0.41), u_* the friction velocity (m s⁻¹), z_l the reference height (here, the altitude of the first model level), z_{0M} and z_{0H} the roughness lengths for heat and momentum, respectively, Ψ_H a stability profile for momentum, and L (m) the Obukhov length calculated using

$$L = -\frac{u_*^3 T_l}{\kappa g Q_{0\nu}}, \quad (\text{A2})$$

with T_l (K) the near-surface air temperature, g (m s⁻²) the gravitational acceleration, and $Q_{0\nu}$ (K m s⁻¹) the virtual temperature flux in the surface layer. The latter depends on the sensible heat flux S (W m⁻²) and evaporation E (kg m⁻² s⁻¹):

$$710 \quad Q_{0\nu} = \frac{S + 0.61 C_p E}{\rho C_p} \quad (\text{A3})$$

with C_p the heat capacity of air (J kg⁻¹ K⁻¹) and ρ the air density (kg m⁻³). Hourly distributions at 0.25° × 0.25° resolution of near-surface temperature, wind, sensible heat flux and evaporation are obtained from the ERA5 reanalysis (Hersbach et al., 2020). Friction velocity is calculated using

$$u_* = \frac{\kappa (u_l^2 + v_l^2 + w_*^2)^{1/2}}{\ln\left(\frac{z_l + z_{0M}}{z_{0M}}\right) - \Psi_M\left(\frac{z_l + z_{0M}}{L}\right) + \Psi_M\left(\frac{z_{0M}}{L}\right)} \quad (\text{A4})$$



715 with u_l and v_l the horizontal wind components at 10 m, and w_* a free convection velocity scale,

$$w_* = (z_i \frac{g}{T_l} Q_{0\nu})^{1/3} \quad (\text{A5})$$

with $z_i = 1000$ m. Since L depends on u_* (Eq. A2) which is dependent on L (Eq. A4), these quantities are calculated iteratively. The stability profiles for heat and momentum follow ECMWF (2021).

The roughness lengths over oceans are calculated (ECMWF, 2021) using

$$z_{0M} = 0.11 \frac{\nu}{u_*} + \alpha_C \frac{u_*^2}{g} \quad (\text{A6})$$

$$z_{0H} = 0.4 \frac{\nu}{u_*} \quad (\text{A7})$$

with ν the kinematic viscosity ($\sim 1.5 \cdot 10^{-5} \text{ m}^2 \text{ s}^{-1}$ at 288 K), and α_C the Charnock dimensionless coefficient provided by the ERA5 reanalysis. Over land, the estimation of z_{0M} follows Zhang et al. (2003), i.e., minimum and maximum values are defined for each plant functional type. The seasonal evolution of the roughness length is based on LAI obtained from monthly averaged Moderate Resolution Imaging Spectroradiometer (MODIS 15A2H collection 6). z_{0H} is assumed equal to $0.1 \cdot z_{0M}$ (ECMWF, 2021).

A2 Quasi-laminar sublayer resistance

Following Toyota et al. (2016), the quasi-laminar sublayer resistance (s m^{-1}) is written as

$$R_b = \frac{1}{B u_*} \left(\frac{\nu}{0.72 D_{g,\text{CH}_3\text{OH}}} \right)^{2/3} \quad (\text{A8})$$

730 where the empirical factor B is taken equal to $\frac{\kappa}{2}$ and $D_{g,\text{CH}_3\text{OH}}$ is the gas-phase diffusivity of methanol, obtained from Tang et al. (2015) ($1.66 \cdot 10^{-5} \text{ m}^2 \text{ s}^{-1}$ at 298 K). The temperature dependence of the diffusivity follows Tang et al. (2015).

A3 Stomatal resistance

R_s is related to the stomatal resistance to the diffusion of water ($R_{\text{H}_2\text{O}}$):

$$R_s = \left(\frac{D_{g,\text{H}_2\text{O}}}{D_{g,\text{CH}_3\text{OH}}} \right) \cdot R_{\text{H}_2\text{O}}, \quad (\text{A9})$$

735 where $D_{g,\text{H}_2\text{O}}$ is the gas-phase diffusivity of water ($2.18 \cdot 10^{-5} \text{ m}^2 \text{ s}^{-1}$ at 298 K, Massman, 1998). The dependence of the stomatal resistance for H_2O on environmental parameters is given (Jarvis, 1976; Sellers et al., 1986) by

$$R_{s,\text{H}_2\text{O}} = \left(\frac{a_s}{b_s + Q} + c_s \right) / (f(T_l) \cdot (1 - d_s \delta_e) \cdot f(\psi_l)), \quad (\text{A10})$$

where Q is the visible radiation flux (W m^{-2}), $f(T_l)$ and $f(\psi_l)$ are stress factors for temperature (T_l) and the leaf water potential (ψ_l), and δ_e is the water vapour deficit (hPa). The stress functions for every plant functional type are detailed in Müller et al. (2008). The values of parameters a_s , b_s , c_s and d_s are given in Table S7. R_s is minimum during daytime, typically of the order of 100 s m^{-1} for ozone (e.g., Baldocchi et al., 1987; Padro, 1996; Val Martin et al., 2016).



A4 Cuticular and soil uptake resistances for SO₂ and O₃

The cuticular resistances for SO₂ and O₃ are calculated (Zhang et al., 2003) with

$$R_{\text{cut}} = \left(\frac{1 - f_{\text{wet}}}{R_{\text{cutd}}} + \frac{f_{\text{wet}}}{R_{\text{cutw}}} \right)^{-1} \quad (\text{A11})$$

745 where f_{wet} is the frequency of wet conditions, due to either dew or rain, and

$$R_{\text{cutd}} = \frac{f_{\text{fr}} \cdot R_{\text{cutd}0}}{e^{0.03 \cdot \text{RH}} \text{LAI}^{0.25} u_*} \quad (\text{A12})$$

$$R_{\text{cutw}} = \frac{f_{\text{fr}} \cdot R_{\text{cutw}0}}{\text{LAI}^{0.5} u_*} \quad (\text{A13})$$

with LAI being relative humidity (in %), f_{fr} a function of temperature, equal to 1 above -1° C, and given by

$$f_{\text{fr}} = \min(2, e^{0.2(-1 - T_C)}) \quad (\text{A14})$$

750 below that temperature. The reference values for dry and wet conditions ($R_{\text{cutd}0}$ and $R_{\text{cutw}0}$) are provided in Table S7 for SO₂ and O₃, except $R_{\text{cutw}0}$, which is equal to 50 s m⁻¹ for rain and 100 s m⁻¹ for dew conditions. Dew presence is assumed to occur when u_* falls below a threshold value dependent on specific humidity and cloud cover (Brook et al., 1999). Rain frequency is estimated from the ERA5 cloud and precipitation fields (Stavrakou et al., 2009c).

755 The ground resistance for SO₂ is taken equal to 50 s m⁻¹ for rain and 100 s m⁻¹ for dew conditions, and is multiplied by the factor f_{fr} . In absence of dew or rain, the ground resistance $R_g^{\text{SO}_2}$ depends on RH and soil pH (Kerkweg et al., 2006). In humid conditions (above 60% RH), the resistance, $R_{g,h}^{\text{SO}_2}$ is taken equal to 115, 65 and 25 s m⁻¹ for pH < 4.0, 5.5 < 7.3 and pH > 7.3, respectively. The soil pH distribution is obtained from Hengl et al. (2017). Below 60% RH, the resistance (s m⁻¹) is calculated by modifying the values for humid conditions ($R_{g,h}^{\text{SO}_2}$) according to

$$R_g^{\text{SO}_2} = \max(25, 3.4 R_{g,h}^{\text{SO}_2} - 85 + 10^5 \cdot \max(0, (40 - \text{RH})/40) + 1000 \cdot e^{269 - T_s}) \quad (\text{A15})$$

760 with T_s the soil temperature (K).

The ground resistance for O₃ is assumed equal to respectively 200 s m⁻¹ under vegetation and 500 s m⁻¹ for non-vegetated surfaces (Zhang et al., 2003). These values are multiplied by f_{fr} (Eq. A14) at low temperatures.

765 Over snow, the ground and cuticular resistance for O₃ are assumed equal to 2000 s m⁻¹; the ground resistance for SO₂ is calculated as function of temperature following Kerkweg et al. (2006). The snow fraction is calculated from the ERA5 snow depth (SD) as the ratio

$$f_{\text{snow}} = \min(1, \frac{\text{SD}}{\text{SD}_{\text{max}}}) \quad (\text{A16})$$

where SD_{max} is taken equal to max(0.02, 0.2 · LAI).

Author contributions. JFM and TS designed the inversions, performed the optimisations and the data analysis and wrote the manuscript. BO contributed to data analysis. BF and LC provided the IASI methanol retrievals and advice on their use. CA, NS and BV provided the



770 Vielsalm and Lonzée data. CV, EM, MM and KS provided the FTIR data and advice on their use. All co-authors read and commented on the manuscript and provided feedback.

Competing interests. The contact author has declared that none of the authors has any competing interests.

775 *Acknowledgements.* This study was supported by the GLANCE project funded by the European Space Agency (ESA) under the “eo science for society” programme and by the CONCERTO project funded by the European Commission under the Horizon Europe programme (grant agreement no. 101185000). L. Clarisse is Senior Research Associate supported by the Belgian F.R.S.-FNRS. E. Mahieu is Research Director with the F.R.S. - FNRS. The FTIR measurements at Jungfraujoch were primarily supported by the F.R.S. - FNRS (Brussels, BE), the GAW-CH program of MeteoSwiss (Zürich, CH) and the HFSJG.ch Foundation (Bern, CH). M. Makarova is supported by a SPbU research project 132392751 (GZ_MDF_2026). The Eureka FTIR measurements were made at the Polar Environment Atmospheric Research Laboratory (PEARL), primarily supported by ECCC, CSA, and NSERC. The Toronto FTIR measurements were made at the University of Toronto 780 Atmospheric Observatory, primarily supported by NSERC and ECCC.



References

Amelynck, C., Laffineur, Q., Schoon, N., and Heinesch, B.: (O)VOC concentration and flux measurements above a mixed forest at the Vielsalm ICOS ecosystem station (Belgium) (Version 1) [Data set]. Royal Belgian Institute for Space Aeronomy, <https://doi.org/10.18758/H659PDR>, 2024a.

785 Amelynck, C., Bachy, A., Schoon, N., and Heinesch, B.: (O)VOC concentration and flux measurements above a maize field at the Lonzée ICOS ecosystem station (Belgium) (Version 1) [Data set]. Royal Belgian Institute for Space Aeronomy. <https://doi.org/10.18758/7V20VH47>, 2024b.

Amelynck, C., Bachy, A., Schoon, N., and Heinesch, B.: (O)VOC concentration and flux measurements above a wheat field at the Lonzée ICOS ecosystem station (Belgium) (Version 1) [Data set]. Royal Belgian Institute for Space Aeronomy. 790 <https://doi.org/10.18758/87DE2ABL>, 2024c.

Andreae, M. O. and Merlet, P.: Emissions of trace gases and aerosols from biomass burning, *Global Biogeochem. Cycles*, 15, 955–966, <https://doi.org/10.1029/2000GB001382>, 2001.

Apel, E. C., Hills, A. J., Lueb, R., Zindel, S., Eisele, S., and Riemer, D. D.: A fast-GC/MS system to measure C₂ to C₄ carbonyls and methanol aboard aircraft, *J. Geophys. Res.*, 108, D208794, <https://doi.org/10.1029/2002JD003199>, 2003.

795 Apel, E. C., Emmons, L. K., Karl, T., Flocke, F., Hills, A. J., Madronich, S., Lee-Taylor, J., Fried, A., Weibring, P., Walega, J., Richter, D., Tie, X., Mauldin, L., Campos, T., Weinheimer, A., Knapp, D., Sive, B., Kleinman, L., Springston, S., Zaveri, R., Ortega, J., Voss, P., Blake, D., Baker, A., Warneke, C., Welsh-Bon, D., de Gouw, J., Zheng, J., Zhang, R., Rudolph, J., Junkermann, W., and Riemer, D. D.: Chemical evolution of volatile organic compounds in the outflow of the Mexico City Metropolitan area, *Atmos. Chem. Phys.*, 10, 2353–2375, <https://doi.org/10.5194/acp-10-2353-2010>, 2010.

800 Apel, E. C., Hornbrook, R. S., Hills, A. J., Blake, N. J., Barth, M. C., Weinheimer, A., Cantrell, C., Rutledge, S. A., Basarab, B., Crawford, J., Diskin, G., Homeyer, C. R., Campos, T., Flocke, F., Fried, A., Blake, D. R., Brune, W., Pollack, I., Peischl, J., Ryerson, T., Wennberg, P. O., Crounse, J. D., Wisthaler, A., Mikoviny, T., Huey, G., Heikes, B., O'Sullivan, D., and Riemer, D. D.: Upper tropospheric ozone production from lightning NO_x -impacted convection: Smoke ingestion case study from the DC3 campaign, *J. Geophys. Res. Atmos.*, 120, 2505–2523, <https://doi.org/10.1002/2014JD022121>, 2015.

805 Archibald, A. T., Petit, A. S., Percival, C. J., Harvey, J. N., Shallcross, D. E.: On the importance of the reaction between OH and RO₂ radicals, *Atmos. Sci. Lett.*, 10, 102–108, <https://doi.org/10.1002/asl.216>, 2009.

Assaf, E., Song, B., Tomas, A., Schoemaecker, C., and Fittschen, C.: The rate constant of the reaction between CH₃O₂ radicals and OH radicals revisited, *J. Phys. Chem. A*, 120, 8923–8932, <https://doi.org/10.1021/acs.jpca.6b07704>, 2016.

810 Assaf, E., Schoemacker, C., Vereecken, L., and Fittschen, C.: Experimental and theoretical investigation of the reaction of RO₂ radicals with OH radicals: Dependence of the HO₂ yield on the size of the alkyl group, *Int. J. Chem. Kinet.*, 50, 670–680, <https://doi.org/10.1002/kin.21191>, 2016.

Bachy, A., Aubinet, M., Amelynck, C., Schoon, N., Bodson, B., Moureux, C., Delaplace, P., De Ligne, A., Heinesch, B.: Methanol exchange dynamics between a temperate cropland soil and the atmosphere, *Atmos. Environ.*, 176, 229–239, <https://doi.org/10.1016/j.atmosenv.2017.12.016>, 2018.

815 Bader, W., Stavrakou, T., Müller, J.-F., Reimann, S., Boone, C. D., Harrisson, J. J., Flock, O., Bovy, B., Franco, B., Lejeune, B., Servais, C., and Mahieu, E.: Long-term evolution and seasonal modulation of methanol above Jungfraujoch (46.5° N, 8.0° E): optimi-



sation of the retrieval strategy, comparison with model simulations and independent observations, *Atmos. Meas. Tech.*, 7, 3861–3872, <https://doi.org/10.5194/amt-7-3861-2014>, 2014.

Baldocchi, D. D., Hicks, B. B., and Camara, P.: A canopy stomatal resistance model for gaseous deposition to vegetated surfaces, *Atmos. Environ.*, 21, 91–101, [https://doi.org/10.1016/0004-6981\(87\)90274-5](https://doi.org/10.1016/0004-6981(87)90274-5), 1987.

Barkley, M. P., Palmer, P. I., De Smedt, I., Karl, T., Guenther, A., and Van Roozendael, M.: Regulated large-scale annual shutdown of Amazonian isoprene emissions?, 36, L04803, <https://doi.org/10.1029/2008GL036843>, 2009.

Barth, M. C., Cantrell, C. A., Brune, W. H., Rutledge, S. A., Crawford, J. H., Huntrieser, H., Carey, L. D., McGorman, D., Weisman, M., Pickering, K. E., Bruning, Anderson, B., Apel, E., Biggerstaff, M., Campos, T., Campuzano-Jost, P., Cohen, R., Crounse, J., Day, D. A., Diskin, G., Flocke, F., Fried, A., Garland, C., Heikes, B., Honomichl, S., Hornbrook, R., Huey, L. G., Jimenez, J. L., Lang, T., Lichtenstein, M., Mikoviny, T., Nault, B., O'Sullivan, D., Pan, L. L., Peischl, J., Pollack, I., Richter, D., Riemer, D., Ryerson, T., Schlager, H., St. Clair, J., Walega, J., Weibring, P., Weinheimer, A., Wennberg, P., WIsthaler, A., Wooldridge, P. J. and Ziegler, C.: The Deep Convective Clouds and Chemistry (DC3) Field Campaign, *Bull. Amer. Meteor. Soc.*, 96, 1281–1309, <https://doi.org/10.1175/BAMS-D-13-00290.1>, 2015.

Bates, K. H., Jacob, D. J., Wang, S., Hornbrook, R. S., Apel, E. C., Kim, M. J., et al.: The global budget of atmospheric methanol: New constraints on secondary, oceanic, and terrestrial sources. *J. Geophys. Res.*, 126, e2020JD033439, <https://doi.org/10.1029/2020JD033439>, 2021.

Bauwens, M., Stavrakou, T., Müller, J.-F., De Smedt, I., Van Roozendael, M., Werf, G. R. van der, Wiedinmyer, C., Kaiser, J. W., Sindelarova, K., and Guenther, A.: Nine years of global hydrocarbon emissions based on source inversion of OMI formaldehyde observations, *Atmos. Chem. Phys.*, 16, 10133–10158, <https://doi.org/10.5194/acp-16-10133-2016>, 2016.

Beaudry, E., Jacob, D. J., Bates, K. H., Zhai, S., Yang, L. H., Pendergrass, D. C., Colombi, N., Simpson, I. J., Wisthaler, A., Hopkins, J. R., and Liao, H.: Ethanol and methanol in South Korea and China: Evidence for large anthropogenic emissions missing from current inventories, *ACS EST Air*, 2, 456–465, <https://doi.org/10.1021/acsestair.4c00210>, 2025.

Brook, J. R., Zhang, L., Di-Giovanni, F., and Padro, J.: Description and evaluation of a model of deposition velocities for routine estimates of air pollutant dry deposition over North America. Part I: model development, *Atmos. Environ.*, 33, 5037–5051, [https://doi.org/10.1016/S1352-2310\(99\)00250-2](https://doi.org/10.1016/S1352-2310(99)00250-2), 1999.

Brune, W. H., Miller, D. O., Thames, A. B., Allen, H. M., Apel, E. C., Blake, D. R., Bui, T. P., Commane, R., Crounse, J. D., Daube, B. C., Dislin, G. S., DiGangi, J. P., Elkins, J. W., Hall, S. R., Hanisco, T. F., Hannum, R. A., Hints, E. J., Hornbrook, R. S., Kim, M. J., McKain, K., Sweeney, C., Teng, A. P., Thompson, C., Ullmann, K., Veres, P. R., Wennberg, P. O., and Wolfe, G. M.: Exploring oxidation in the remote free troposphere: Insights from Atmospheric Tomography (ATom), *J. Geophys. Res. Atmos.*, 125, e2019JD031685, <https://doi.org/10.1029/2019JD031685>, 2020.

Burkholder, J. B., Sander, S. P., Abbatt, J. P. D., Barker, J. R., Cappa, C., Crounse, J. D., Dibble, T. S., Huie, R. E., Kolb, C. E., Kurylo, M. J., Orkin, V. L., Percival, C. J., Wilmouth, D. M., and Wine, P. H.: Chemical Kinetics and Photochemical Data for Use in Atmospheric Studies – Evaluation Number 19, Jet Propulsion Laboratory, California Institute of Technology, Pasadena, California, available at: <http://jpldataeval.jpl.nasa.gov> (last access: 16 January 2026), 2020.

Cady-Pereira, K. E., Shephard, M. W., Millet, D. B., Luo, M., Wells, K. C., Xiao, Y., Payne, V. H., and Worden, J.: Methanol from TES global observations: retrieval algorithm and seasonal and spatial variability, *Atmos. Chem. Phys.*, 12, <https://doi.org/10.5194/acp-12-8189-2012>, 2012.

Caravan, R. L., Khan, M. A. H., Z'ador, J., Sheps, L., Antonov, I. O., Rotavera, B., Ramasesha K. Au, K., Chen, M.-W., Rösch, D., Osborn, D. L., Fittschen, C., Schoemaecker, C., Duncianu, M., Frira, A., Dusanter, S., Tomas, A., Percival, C. J., Shallcross, D. E., and Taatjes,



855 C. A.: The reaction of hydroxyl and methylperoxy radicals is not a major source of atmospheric methanol, *Nat. Commun.*, 9, 4343, <https://doi.org/10.1038/s41467-018-06716-x>, 2018.

860 Chen, X., Millet, D. B., Singh, H. B., Wisthaler, A., Apel, E. C., Atlas, E. L., Blake, D. R., Brown, S. S., Crounse, J. D., de Gouw, J. A., Flocke, F., Fried, A., Heikes, B. G., Hornbrook, R. S., Mikoviny, T., Min, K.-E., Müller, M., Neuman, J. A., O'Sullivan, D. W., Peischl, J., Pfister, G. G., Richter, D., Roberts, J. M., Ryerson, T. B., Shertz, S., Treadaway, V., Veres, P. R., Walega, J., Warneke, C., Washenfelder, R. A., Weibring, P., and Yuan, B.: On the sources and sinks of atmospheric VOCs: An integrated analysis of recent aircraft campaigns over North America, *Atmos. Chem. Phys.*, 19, 9097–9123, <https://doi.org/10.5194/acp-19-9097-2019>, 2019.

865 Clarisse, L., Franco, B., Van Damme, M., Di Gioacchino, T., Hadji-Lazaro, J., Whitburn, S., Noppen, L., Hurtmans, D., Clerbaux, C., and Coheur, P.: The IASI NH₃ version 4 product: averaging kernels and improved consistency, *Atmos. Meas. Tech.*, 16, 5009–5028, <https://doi.org/10.5194/amt-16-5009-2023>, 2023.

870 Crawford, J. H., Ahn, J.-Y., Al-Saadi, J., Chang, L., Emmons, L. K., Kim, J., Lee, G., Park, J.-H., Park, R. J., Woo, J. H., Song, C.-K., Hong, J.-H., Hong, Y.-D., Lefer, B. L., Lee, M., Lee, T., Kim, S., Min, K.-E., Yum, S. S., Shin, H. J., Kim, Y.-W., Choi, J.-S., Park, J.-S., Szykman, J. J., Long, R. W., Jordan, C. E., Simpson, I. J., Fried, A., Dibb, J. E., Cho, S., and Kim, Y. P.: The Korea-United States Air Quality (KORUS-AQ) field study, *Elem. Sci. Anth.*, 9(1), 00163, <https://doi.org/10.1525/elementa.2020.00163>, 2021.

875 Davison, B., Brunner, A., Ammann, C., Spirig, C., Jocher, M., and Neftel, A.: Cut-induced VOC emissions from agricultural grasslands, *Plant Biol.*, 10, 76–85, <https://doi.org/10.1055/s-2007-965043>, 2008.

880 de Gouw, J., and Warneke, C.: Measurements of volatile organic compounds in the earth's atmosphere using proton-transfer-reaction mass spectrometry, *Mass Spectrom. Rev.*, 26, 223–257, <https://doi.org/10.1002/mas.20119>, 2007.

885 De Mazière, M., Thompson, A. M., Kurylo, M. J., Wild, J. D., Bernhard, G., Blumenstock, T., Braathen, G. O., Hannigan, J. W., Lambert, J.-C., Leblanc, T., McGee, T. J., Nedoluha, G., Petropavlovskikh, I., Seckmeyer, G., Simon, P. C., Steinbrecht, W., and Strahan, S. E.: The Network for the Detection of Atmospheric Composition Change (NDACC): history, status and perspectives, *Atmos. Chem. Phys.*, 18, 4935–4964, <https://doi.org/10.5194/acp-18-4935-2018>, 2018.

890 De Smedt, I., Pinardi, G., Vigouroux, C., Compernolle, S., Bais, A., Benavent, N., Boersma, F., Chan, K.-L., Donner, S., Eichmann, K.-U., Hedelt, P., Hendrick, F., Irie, H., Kumar, V., Lambert, J.-C., Langerock, B., Lerot, C., Liu, C., Loyola, D., Piters, A., Richter, A., Rivera Cárdenas, C., Romahn, F., Ryan, R. G., Sinha, V., Theys, N., Vlietinck, J., Wagner, T., Wang, T., Yu, H., and Van Roozendael, M.: Comparative assessment of TROPOMI and OMI formaldehyde observations and validation against MAX-DOAS network column measurements, *Atmos. Chem. Phys.*, 21, 12561–12593, <https://doi.org/10.5194/acp-21-12561-2021>, 2021.

900 ECMWF (European Centre for Medium-range Weather Forecasts): IFS Documentation - Cy47r3 Operational implementation. Part IV: Physical Processes, European Centre for Medium-Range Weather Forecasts, Shinfield Park, Reading, RG2 9AX, England, <https://doi.org/10.21957/eyrpir4vj>, 2021.

905 Eskes, H., and Boersma, K. F.: Averaging kernels for DOAS total-column satellite retrievals, *Atmos. Chem. Phys.*, 3, 1285–1291, <https://doi.org/10.5194/acp-3-1285-2003>, 2003.

910 Fall, R., and Benson, A. A.: Leaf methanol – the simplest natural product from plants, *Trends Plant. Sci.*, 1, 296–301, [https://doi.org/10.1016/S1360-1385\(96\)88175-0](https://doi.org/10.1016/S1360-1385(96)88175-0), 1996.

915 Franco, B., Clarisse, L., Stavrakou, T., Müller, J. -F., Van Damme, M., Whitburn, S., Hadji-Lazaro, J., Hurtmans, D., Taraborrelli, D., Clerbaux, C., and Coheur, P. -F.: A general framework for global retrievals of trace gases from IASI: Application to methanol, formic acid, and PAN, *J. Geophys. Res.-Atmos.*, 123, 13,963–13,984, <https://doi.org/10.1029/2018JD029633>, 2018.



Franco, B., Clarisso, L., Stavrakou, T., Müller, J. -F., Pozzer, A., Hadji-Lazaro, J., Hurtmans, D., Clerbaux, C., and Coheur, P. -F.: Acetone atmospheric distribution retrieved from space, *Geophys. Res. Lett.*, 46, 2884–2893, <https://doi.org/10.1029/2019GL082052>, 2019.

Franco, B., Clarisso, L., Stavrakou, T., Müller, J.-F., Taraborrelli, D., Hadji-Lazaro, J., Hannigan, J. W., Hase, F., Hurtmans, D.,
895 Jones, N., Lutsch, E., Mahieu, E., Ortega, I., Schneider, M., Strong, K., Vigouroux, C., Clerbaux, C., and Coheur, P.-F.: Space-
borne measurements of formic and acetic acid: A global view of the regional sources, *Geophys. Res. Lett.*, 47, e2019GL086239,,
<https://doi.org/10.1029/2019GL086239>, 2020.

Franco, B., Clarisso, L., Theys, N., Hadji-Lazaro, J., Clerbaux, C., and Coheur, P.: Pyrogenic HONO seen from space: Insights from global
IASI observations, *Atmos. Chem. Phys.*, 24, 4973–5007. <https://doi.org/10.5194/acp-24-4973-2024>, 2024.

900 Gao, W., and Wesely, M. L.: Modeling gaseous dry deposition over regional scales with satellite observations – I. Model development,
Atmos. Environ., 29, 727–737, [https://doi.org/10.1016/1352-2310\(94\)00284-R](https://doi.org/10.1016/1352-2310(94)00284-R), 1995.

Guenther, A., Karl, T., Harley, P., Wiedinmyer, C., Palmer, P. I., and Geron, C.: Estimates of global terrestrial isoprene emissions using
MEGAN (Model of Emissions of Gases and Aerosols from Nature), *Atmos. Chem. Phys.*, 6, 3181–3210, <https://doi.org/10.5194/acp-6-3181-2006>, 2006.

905 Guenther, A. B., Jiang, X., Heald, C. L., Sakulyanontvittaya, T., Duhl, T., Emmons, L. K., and Wang, X.: The Model of Emissions of Gases
and Aerosols from Nature version 2.1 (MEGAN2.1): an extended and updated framework for modeling biogenic emissions, *Geosci. Model
Dev.*, 5, 1471–1492, <https://doi.org/10.5194/gmd-5-1471-2012>, 2012.

Heikes, B. G., Chang, W., Pilson, M. E. Q., Swift, E., Singh, H. B., Guenther, A., Jacob, D. J., Field, B. D., Fall, R., Riemer, D., and Brand,
L.: Atmospheric methanol budget and ocean implication, *Global Biogeochem. Cycles*, 16, 1133, <https://doi.org/10.1029/2002GB001895>,
910 2002.

Hengl, T., Mendes de Jesus, J., Heuvelink, G. B. M., Ruiperez Gonzalez, M., Kilibarda, M., Blagotić, A., Wei Shangguan, W., Wright, M. N.,
Geng, X., Bauer-Marschallinger, B., Antonio Guevara, M., Vargas, R., MacMillan, R. A., Batjes, N. H., Leenaars, J. G. B., Eloi Ribeiro,
R., Wheeler, I., Mantel, S., Kempen, B.: SoilGrids250m: Global gridded soil information based on machine learning, *PLoS ONE*, 12,
e0169748, <https://doi.org/10.1371/journal.pone.0169748>, 2017.

915 Hersbach, H., Bell, B., Berrisford, P., Hirahara, S., Horányi, A., Muñoz-Sabater, J., Nicolas, J., Peubey, C., Radu, R., Schepers, D., Simmons,
A., Soci, C., Abdalla, S., Abellan, X., Balsamo, G., Bechtold, P., Biatovi, G., Bidlot, J., Bonavita, M., De Chiara, G., Dahlgren, P., Dee,
D., Diamantakis, M., Dragani, R., Flemming, J., Forbes, R., Fuentes, M., Geer, A., Haimberger, L., Healy, S., Hogan, R. J., Hólm, E.,
Janisková, M., Keeley, S., Laloyaux, P., Lopez, P., Lupu, C., Radnoti, G., de Rosnay, P., Rozum, I., Vamborg, F., Villaume, S., and Thépaut,
J.-N.: The ERA5 global reanalysis, *Q. J. R. Meteorol. Soc.*, 146, 1999–2049, <https://doi.org/10.1002/qj.3803>, 2020.

920 Hu, L., Millet, D. B., Mohr, M. J., Wells, K. C., Griffis, T. J., and Helmig, D.: Sources and seasonality of atmospheric methanol based on tall
tower measurements in the US Upper Midwest, *Atmos. Chem. Phys.*, 11, 11145–11156, doi:10.5194/acp-11-11145-2011, 2011.

Huang, G., Brook, R., Crippa, M., Janssens-Maenhout, G., Schieberle, C., Dore, C., Guizzardi, D., Muntean, M., Schaaf, E., and Friedrich,
R.: Speciation of anthropogenic emissions of non-methane volatile organic compounds: a global gridded data set for 1970–2012, *Atmos.
Chem. Phys.*, 17, 7683–7701, <https://doi.org/10.5194/acp-17-7683-2017>, 2017.

925 Jacob, D. J., Field, B. D., Li, Q., Blake, D. R., de Gouw, J. and Warneke, C., Hansel, A., Wisthaler, A., Singh, H. B., and Guenther, A.: Global
budget of methanol: Constraints from atmospheric observations, *J. Geophys. Res.*, 110, D08303, <https://doi.org/10.1029/2004JD005172>,
2005.

Jacob, D. J., Crawford, J. H., Maring, H., Clarke, A. D., Dibb, J. E., Emmons, L. K., Ferrare, R. A., Hostetler, C. A., Russell, P. B., Singh,
H. B., Thompson, A. M., Shaw, G. E., McCauley, E., Pederson, J. R., and Fisher, J. A.: The Arctic Research of the Composition of the



930 Troposphere from Aircraft and Satellites (ARCTAS) mission: design, execution, and first results, *Atmos. Chem. Phys.*, 10, 5191–5212, <https://doi.org/10.5194/acp-10-5191-2010>, 2010.

Janssens-Maenhout, G., Crippa, M., Guizzardi, D., Dentener, F., Muntean, M., Pouliot, G., Keating, T., Zhang, Q., Kurokawa, J., Wankmüller, R., Denier van der Gon, H., Kuenen, J. J. P., Klimont, Z., Frost, G., Darras, S., Koffi, B., and Li, M.: HTAP_v2.2: a mosaic of regional and global emission grid maps for 2008 and 2010 to study hemispheric transport of air pollution, *Atmos. Chem. Phys.*, 15, 11411–11432, <https://doi.org/10.5194/acp-15-11411-2015>, 2015.

935 Jarvis, P.: The interpretation of the variations in leaf water potential and stomatal conductance found in canopies in the field, *Phil. Trans. Roy. Soc. London, B*, 273, 593–610, <https://doi.org/10.1098/rstb.1976.0035>, 1976.

Johnson, M. T.: A numerical scheme to calculate temperature and salinity dependent air-water transfer velocities for any gas, *Ocean Sci.*, 6, 913–932, <https://doi.org/10.5194/os-6-913-2010>, 2010.

940 Kerkweg, A., Buchholz, J., Ganzeveld, L., Pozzer, A., Tost, H., and Jöckel, P.: Technical note: An implementation of the dry removal processes DRY DEPosition and SEDImentation in the Modular Earth Submodel System (MESSy), *Atmos. Chem. Phys.*, 6, 4617–4632, <https://doi.org/10.5194/acp-6-4617-2006>, 2006.

Khan, M., Cooke, M., Utembe, S., Xiao, P., Derwent, R., Jenkin, M., Archibald, A. T., Maxwell, P., Morris, W. C., South, N., Percival, C. J., and Shallcross, D. E.: Reassessing the photochemical production of methanol from peroxy radical self and cross reactions using 945 the STOCHEM-CRI global chemistry and transport model, *Atmos. Environ.*, 99, 77–84. <https://doi.org/10.1016/j.atmosenv.2014.09.056>, 2014.

Khan, M., Cooke, M., Utembe, S., Archibald, A. T., Derwent, R. G. and Jenkin, M. E., Morris, W. C., South, N., Hansen, J. C., Francisco, J. S., Percival, C. J., and Shallcross, D. E.: Global analysis of peroxy radicals and peroxy radical-water complexation using the STOCHEM-CRI global chemistry and transport model, *Atmos. Environ.*, 106, 278–287, <https://doi.org/10.1016/j.atmosenv.2015.02.020>, 2015.

950 Laffineur, Q., Aubinet, M., Schoon, N., Amelynck, C., Müller, J.-F., Dewulf, J., Van Langenhove, H., Steppe, K., and Heinesch, B.: Abiotic and biotic control of methanol exchanges in a temperate mixed forest, *Atmos. Chem. Phys.*, 12, 577–590, <https://doi.org/10.5194/acp-12-577-2012>, 2012.

Langford, B., Misztal, P. K., Nemitz, E., Davison, B., Helfter, C., Pugh, T. A. M., MacKenzie, A. R., Lim, S. F., and Hewitt, C. N.: Fluxes and concentrations of volatile organic compounds from a South-East Asian tropical rainforest, *Atmos. Chem. Phys.*, 10, 8391–8412, <https://doi.org/10.5194/acp-10-8391-2010>, 2010.

955 Lindinger, W., Hansel, A., and Jordan, A.: On-line monitoring of volatile organic compounds at pptv levels by means of proton-transfer-reaction mass spectrometry (PTR-MS) – Medical applications, food control and environmental research, *Int. J. Mass Spectrom.*, 173, 191–241, [https://doi.org/10.1016/S0168-1176\(97\)00281-4](https://doi.org/10.1016/S0168-1176(97)00281-4), 1998.

Madronich, S., and Calvert, J. G.: Permutation reactions of organic peroxy radicals in the troposphere, *J. Geophys. Res.*, 95, 5697–5715, <http://dx.doi.org/10.1029/JD095iD05p05697>, 1990.

960 Madronich, S. and Flocke, S.: The role of solar radiation in atmospheric chemistry, in: *Handbook of Environmental Chemistry*, edited by: Boule, P., Springer Verlag, Heidelberg, 1–26, https://doi.org/10.1007/978-3-540-69044-3_1, 1998.

Martin, S. T., Artaxo, P., Machado, L. A. T., Manzi, A. O., Souza, R. A. F., Schumacher, C., Wang, J., Andreae, M. O., Barbosa, H. M. J., Fan, J., Disch, J., Goldstein, A. H., Guenther, A., Jimenez, J. L., Pöschl, U., Silva Dias, M. A., Smith, J. N., and Wendisch, M.: Introduction: Observations and Modeling of the Green Ocean Amazon (GoAmazon2014/5), *Atmos. Chem. Phys.*, 16, 4785–4797, <https://doi.org/10.5194/acp-16-4785-2016>, 2016.



Massman, W. J.: A review of the molecular diffusivities of H₂O, CO₂, CH₄, CO, O₃, SO₂, NH₃, N₂O, NO, and NO₂ in air, O₂ and N₂ near STP, *Atmos. Environ.*, 32, 1111–1127, [https://doi.org/10.1016/S1352-2310\(97\)00391-9](https://doi.org/10.1016/S1352-2310(97)00391-9), 1998.

Millet, D. B., Jacob, D. J., Turquety, S., Hudman, R. C., Wu, S., Fried, A., Walega, J., Heikes, B. G., Blake, D. R., Singh, H. B., Anderson, B. E. and Clarke, A. D.: Formaldehyde distribution over North America: Implications for satellite retrievals of formaldehyde columns and isoprene emission, *J. Geophys. Res.*, 111, D24S02, <https://doi.org/10.1029/2005JD006853>, 2006.

Millet, D. B., Jacob, D. J., Custer, T. G., de Gouw, J. A., Goldstein, A. H., Karl, T., Singh, H. B., Sive, B. C., Talbot, R. W., Warneke, C., and Williams, J.: New constraints on terrestrial and oceanic sources of atmospheric methanol, *Atmos. Chem. Phys.*, 8, 6887–6905, <https://doi.org/10.5194/acp-8-6887-2008>, 2008.

Müller, M., Mikoviny, T., Feil, S., Haidacher, S., Hanel, G., Hartungen, E., Jordan, A., Märk, L., Mutschlechner, P., Schottkowsky, R., Sulzer, R., Crawford, J. H., and Wisthaler, A.: A compact PTR-ToF-MS instrument for airborne measurements of volatile organic compounds at high spatiotemporal resolution, *Atmos. Meas. Tech.*, 7, 3763–3772, <https://doi.org/10.5194/amt-7-3763-2014>, 2014.

Müller, J.-F., Stavrakou, T., Wallens, S., De Smedt, I., Van Roozendael, M., Rinne, J., Munger, B., Goldstein, A., and Guenther, A.: Global isoprene emissions estimated using MEGAN, ECMWF analyses and a detailed canopy environmental model, *Atmos. Chem. Phys.*, 8, 1329–1341, <https://doi.org/10.5194/acp-8-1329-2008>, 2008.

Müller, J.-F., Liu, Z., Nguyen, V. S., Stavrakou, T., Harvey, J. N., and Peeters, J.: The reaction of methyl peroxy and hydroxyl radicals as a major source of atmospheric methanol, *Nat. Commun.*, 7, 13213. <https://doi.org/10.1038/ncomms13213>, 2016.

Müller, J.-F., Stavrakou, T., and Peeters, J.: Chemistry and deposition in the Model of Atmospheric composition at Global and Regional scales using Inversion Techniques for Trace gas Emissions (MAGRITTE v1.1). Part A. Chemical mechanism, *Geosci. Model Dev.*, 12, 2307–2356, <https://doi.org/10.5194/gmd-12-2307-2019>, 2019.

Müller, J.-F., Stavrakou, T., Oomen, G.-M., Opacka, B., De Smedt, I., Guenther, A., Vigouroux, C., Langerock, B., Aquino, C. A. B., Grutter, M., Hannigan, J., Hase, F., Kivi, R., Lutsch, E., Mahieu, E., Makarova, M., Metzger, J.-M., Morino, I., Murata, I., Nagahama, T., Notholt, J., Ortega, I., Palm, M., Röhling, A., Stremme, W., Strong, K., Sussmann, R., Té, Y., and Fried, A.: Bias correction of OMI HCHO columns based on FTIR and aircraft measurements and impact on top-down emission estimates, *Atmos. Chem. Phys.*, 24, 2207–2237, <https://doi.org/10.5194/acp-24-2207-2024>, 2024.

Müller, J.-F., and Stavrakou, T.: Global top-down methanol emissions based on IASI data (2008–2019) (Version 1) [Data set], Royal Belgian Institute for Space Aeronomy, <https://doi.org/10.18758/5FMK39FW>, 2026.

NASA: NASA Tropospheric Chemistry Campaigns – Merged Data Sets, NASA [data set], <https://www-air.larc.nasa.gov/missions/merges> (last access: 16 January 2026), 2025.

Nemecek-Marshall, M., MacDonald, R. C., Franzen, J. J., Wojciechowski, C. L., and Fall, R.: Methanol emission from leaves (Enzymatic detection of gas-phase methanol and relation of methanol fluxes to stomatal conductance and leaf development), *Plant Physiol.*, 108, 1359–1368, <https://doi.org/10.1104/pp.108.4.1359>, 1995.

Nightingale, P. D., Malin, G., Law, C. S., Watson, A. J., Liss, P. S., Liddicoat, M. I., Boutin, J., and Upstill-Goddard, R. C.: In situ evaluation of air-sea gas exchange parameterizations using novel conservative, volatile tracers, *Global Biogeochem. Cycles*, 14, 373–387, <https://doi.org/10.1029/1999GB900091>, 2000.

Oomen, G.-M., Müller, J.-F., Stavrakou, T., De Smedt, I., Blumenstock, T., Kivi, R., Makarova, M., Palm, M., Röhling, A., Té, Y., Vigouroux, C., Friedrich, M. M., Frieß, U., Hendrick, F., Merlaud, A., Piters, A., Richter, A., Van Roozendael, M., and Wagner, T.: Weekly derived top-down volatile-organic-compound fluxes over Europe from TROPOMI HCHO data from 2018 to 2021, *Atmos. Chem. Phys.*, 24, 449–474, <https://doi.org/10.5194/acp-24-449-2024>, 2024.



1005 Padro, J.: Summary of ozone dry deposition velocity measurements and model estimates over vineyard, grass and deciduous forest in summer, *Atmos. Environ.*, 30, 2363–2369, [https://doi.org/10.1016/1352-2310\(95\)00352-5](https://doi.org/10.1016/1352-2310(95)00352-5), 1996.

Peñuelas, J., Asensio, D., Tholl, D., Wenke, K., Rosenkranz, M., Piechulla, B., and schnitzler, J. P.: Biogenic volatile emissions from the soil, *Plant Cell Environ.*, 37, 1866–1891, <https://doi.org/10.1111/pce.12340>, 2014.

Rantala, P., Aalto, J., Taipale, R., Ruuskanen, T., and Rinne, J.: Annual cycle of volatile organic compound exchange between a boreal pine forest and the atmosphere, *Biogeosciences*, 12, 5723–5770, <https://doi.org/10.5194/bg-12-5753-2015>, 2015.

1010 Razavi, A., Karagulian, F., Clarisse, L., Hurtmans, D., Coheur, P.-F., Clerbaux, C., Müller, J.-F., and Stavrakou, T.: Global distributions of methanol and formic acid retrieved for the first time from the IASI/MetOp thermal infrared sounder, *Atmos. Chem. Phys.*, 11, 857–872, <https://doi.org/10.5194/acp-11-857-2011>, 2011.

Read, K. A., Carpenter, L. J., Arnold, S. R., Beale, R., Nightingale, P D., Hopkins, J. R., Lewis, A. C., Lee, J. D., Mendes, L., and Pickering, S. J.: Multiannual observations of acetone, methanol, and acetaldehyde in remote Tropical Atlantic air: Implications for atmospheric OVOC budgets and oxidative capacity, *Environ. Sci. Technol.*, 46, 11028–11039, <https://doi.org/10.1021/es302082p>, 2012.

Rinsland, C. P., Mahieu, E., Chiou, L., and Herbin, H.: First ground-based infrared solar absorption measurements of free tropospheric methanol (CH_3OH): Multidecade infrared time series from Kitt Peak (31.9°N 111.6°W): Trend, seasonal cycle, and comparison with previous measurements, *J. Geophys. Res.*, 114, D04309, <https://doi.org/10.1029/2008JD011003>, 2009.

1015 Sander, R.: Compilation of Henry's law constants (version 4.0), *Atmos. Chem. Phys.*, 15, 4399–4981, <https://doi.org/10.5194/acp-15-4399-2015>, 2015.

Sellers, P., Mintz, Y., Sud, Y., and Dalcher, A.: A Simple Biosphere Model (SiB) for Use within General Circulation Models, *J. Atmos. Sci.*, 43, 505–531, [https://doi.org/10.1175/1520-0469\(1986\)043<0505:ASBMFU>2.0.CO;2](https://doi.org/10.1175/1520-0469(1986)043<0505:ASBMFU>2.0.CO;2), 1986.

Singh, H. B., Chen, Y., Staudt, A., Jacob, D., Blake, D., Heikes, B., and Snow, J.: Evidence from the Pacific troposphere for large global 1020 sources of oxygenated organic compounds, *Nature*, 410, 1078–1081, <https://doi.org/10.1038/35074067>, 2001.

Sindelarova, K., Granier, C., Bouarar, I., Guenther, A., Tilmes, S., Stavrakou, T., Müller, J.-F., Kuhn, U., Stefani, P., and Knorr, W.: Global data set of biogenic VOC emissions calculated by the MEGAN model over the last 30 years, *Atmos. Chem. Phys.*, 14, 9317–9341, <https://doi.org/10.5194/acp-14-9317-2014>, 2014.

Sindelarova, K., Markova, J., Simpson, D., Huszar, P., Karlicky, J., Darras, S., and Granier, C.: High resolution biogenic global emission 1025 inventory for the time period 2000–2019 for air quality modelling, *Earth Syst. Sci. Data*, 14, 251–270, <https://doi.org/10.5194/essd-14-251-2022>, 2022.

Sofiev, M., Vankevich, R., Ermakova, T., and Hakkarainen, J.: Global mapping of maximum emission heights and resulting vertical profiles of wildfire emissions, *Atmos. Chem. Phys.*, 13, 7039–7052, <https://doi.org/10.5194/acp-13-7039-2013>, 2013.

Souri, A. H., Gonález Abad, G., Wolfe, G. M., Verhoelst, T., Vigouroux, C., Pinardi, G., Compernolle, S., Langerock, B., Duncan, B. N., and 1030 Johnson, M. S.: Feasibility of robust estimates of ozone production rates using a synergy of satellite observations, ground-based remote sensing, and models, *Atmos. Chem. Phys.*, 25, 2061–2086, <https://doi.org/10.5194/acp-25-2061-2025>, 2025.

Stavrakou, T., Müller, J.-F., De Smedt, I., Van Roozendael, M., van der Werf, G. R., Giglio, L., and Guenther, A.: Evaluating the performance of pyrogenic and biogenic emission inventories against one decade of space-based formaldehyde columns, *Atmos. Chem. Phys.*, 9, 1037–1060, <https://doi.org/10.5194/acp-9-1037-2009>, 2009a.

1040 Stavrakou, T., Müller, J.-F., De Smedt, I., Van Roozendael, M., Kanakidou, M., Vrekoussis, M., Wittrock, F., Richter, A., and Burrows, J. P.: The continental source of glyoxal estimated by the synergistic use of spaceborne measurements and inverse modelling, *Atmos. Chem. Phys.*, 9, 8431–8446, <https://doi.org/10.5194/acp-9-8431-2009>, 2009b.



1045 Stavrakou, T., Guenther, A., Razavi, A., Clarisse, L., Clerbaux, C., Coheur, P.-F., Hurtmans, D., Karagulian, F., De Mazière, M., Vigouroux, C., Amelynck, C., Schoon, N., Laffineur, Q., Heinesch, B., Aubinet, M., Rinsland, C., and Müller, J.-F.: First space-based derivation of the global atmospheric methanol emission fluxes, *Atmos. Chem. Phys.*, 11, 4873–4898, <https://doi.org/10.5194/acp-11-4873-2011>, 2011.

1050 Tang, M. J., Shiraiwa, M., Pöschl, U., Cox, R. A., and Kalberer, M.: Compilation and evaluation of gas phase diffusion coefficients of reactive trace gases in the atmosphere: Volume 2. Diffusivities of organic compounds, pressure-normalised mean free paths, and average Knudsen numbers for gas uptake calculations, *Atmos. Chem. Phys.*, 15, 5585–5598, <https://doi.org/10.5194/acp-15-5585-2015>, 2015.

Tie, X. T., Guenther, A., and Holland, E.: Biogenic methanol and its impacts on tropospheric oxidants, *Geophys. Res. Lett.*, 30, 1881, <https://doi.org/10.1029/2003GL017167>, 2003.

1055 Toyota, K., Dastoor, A. P., and Ryzhkov: A. Parameterization of gaseous dry deposition in atmospheric chemistry models: Sensitivity to aerodynamic resistance formulations under statically stable conditions, *Atmos. Environ.*, 147, 409–422, <https://doi.org/10.1016/j.atmosenv.2016.09.055>, 2016.

Toon, O. B., Maring, H., Dibb, J., Ferrare, R., Jacob, D. J., Jensen, E. J., Luo, Z. J., Mace, G. G., Pan, L. L., Pfister, L., Rosenlof, K. H., Redemann, J., Reid, J. S., Singh, H. B., Yokelson, R., Minnis, P., Chen, G., Jucks, K. W., and Pszenny, A.: Planning, implementation and scientific goals of the Studies of Emissions and Atmospheric Composition, Clouds and Climate Coupling by Regional Survey (SEAC⁴RS) field mission, *J. Geophys. Res.*, 121, 4967–5009, <https://doi.org/10.1002/2015JD024297>, 2016.

Val Martin, M., Heald, C. L., and Arnold, S. R.: Coupling dry deposition to vegetation phenology in the Community Earth System Model: Implications for the simulations of surface O₃, *Geophys. Res. Lett.*, 41, 2988–2996, <https://doi.org/10.1002/2014GL059651>, 2016.

1060 van der Werf, G. R., Randerson, J. T., Giglio, L., van Leeuwen, T. T., Chen, Y., Rogers, B. M., Mu, M., van Marle, M. J. E., Morton, D. C., Collatz, G. J., Yokelson, R. J., and Kasibhatla, P. S.: Global fire emissions estimates during 1997–2016, *Earth Syst. Sci. Data*, 9, 697–720, <https://doi.org/10.5194/essd-9-697-2017>, 2017.

Viatte, C., Strong, K., Walker, K. A., and Drummond, J. R.: Five years of CO, HCN, C₂H₆, C₂H₂, CH₃OH, HCOOH and H₂CO total columns measured in the Canadian high Arctic, *Atmos. Meas. Tech.*, 7, 1547–1570, <https://doi.org/10.5194/amt-7-1547-2014>, 2014.

1065 Vigouroux, C., Stavrakou, T., Whaley, C., Dils, B., Duflot, V., Hermans, C., Kumps, N., Metzger, J.-M., Scolas, F., Vanhaelewijn, G., Müller, J.-F., Jones, D. B. A., Li, Q., and De Mazière, M.: FTIR time-series of biomass burning products (HCN, C₂H₆, C₂H₂, CH₃OH, and HCOOH) at Reunion Island (21° S, 55° E) and comparisons with model data, *Atmos. Chem. Phys.*, 12, 10367–10385, <https://doi.org/10.5194/acp-12-10367-2012>, 2012.

Vigouroux, C., Langerock, B., Aquino, C. A. B., Blumenstock, T., De Mazière, M., De Smedt, I., Grutter, M., Hannigan, J., Jones, N., Kivi, R., Lutsch, E., Mahieu, E., Makarova, M., Metzger, J.-M., Morin, I., Murata, I., Nagahama, T., Notholt, J., Ortega, I., Palm, M., Pinardi, G., Röhling, A., Smale, D., Stremme, W., Strong, K., Sussmann, R., Té, Y., Van Roozendael, M., Wang, P., and Winkler, H.: TROPOMI/S5P formaldehyde validation using an extensive network of ground-based FTIR stations, *Atmos. Meas. Tech.*, 3751–3767, <https://doi.org/10.5194/amt-13-3751-2020>, 2020.

1070 Warneke, C., Karl, T., Judmaier, H., Hansel, A., Jordan, A., Lindigner, W., and Crutzen, P.: Acetone, methanol, and other partially oxidized volatile organic emissions from dead plant matter by abiological processes: Significance for atmospheric HO_x chemistry, *Global Biogeochem. Cy.*, 13, 9–17, <https://doi.org/10.1029/98GB02428>, 1999.

Warneke, C., Trainer, M., de Gouw, J. A., Parrish, D. D., Fahey, D. W., Ravishankara, A. R., Middlebrook, A. M., Brock, C. A., Roberts, J. M., Brown, S. S., Neuman, J. A., Lerner, B. M., Lack, D., Law, D., Hübler, G., Pollack, I., Sjostedt, S., Ryerson, T. B., Gilman, J. B., Liao, J., Holloway, J., Peischl, J., Nowak, J. B., Aikin, K. C., Min, K.-E., Washenfelder, R. A., Graus, M. G., Richardson, M., Markovic, M. Z., Wagner, N. L., Welti, A., Veres, P. R., Edwards, P., Schwarz, J. P., Gordon, T., Dube, W. P., McKeen, S. A., Brioude, J., Ahmadov, 1075



R., Bougiatioti, A., Lin, J. J., Nenes, A., Wolfe, G. M., Hanisco, T. F., Lee, B. H., Lopez-Hilfiker, F. D., Thornton, J. A., Keutsch, F. N., Kaiser, J., Mao, J., and Hatch, C. D.: Instrumentation and measurement strategy for the NOAA SENEX aircraft campaign as part of the Southeast Atmosphere Study 2013, *Atmos. Meas. Tech.*, 9, 3063–3093, <https://doi.org/10.5194/amt-9-3063-2016>, 2016.

Wells, K. C., Millet, D. B., Hu, L., Cady-Pereira, K. E., Xiao, Y., Shephard, M. W., Clerbaux, C. L., Clarisse, L., Coheur, P.-F., Apel, E. C., de Gouw, J., Warneke, C., Singh, H. B., Goldstein, A. H., and Sive, B. C.: Tropospheric methanol observations from space: retrieval evaluation and constraints on the seasonality of biogenic emissions, *Atmos. Chem. Phys.*, 12, 5897–5912, <https://doi.org/10.5194/acp-12-5897-2012>, 2012.

Wells, K. C., Millet, D. B., Cady-Pereira, K. E., Shephard, M. W., Henze, D. K., Bouscerez, N., Apel, E. C., de Gouw, J. A., Warneke, C., and Singh, H. B.: Quantifying global terrestrial methanol emissions using observations from the TES satellite sensor, *Atmos. Chem. Phys.*, 14, 2555–2570, <https://doi.org/10.5194/acp-14-2555-2014>, 2014.

Wells, K. C., Millet, D. B., Brewer, J. F., Payne, V. H., Cady-Pereira, K., Pernak, R., Kulawik, S., Vigouroux, C., Jones, N., Mahieu, E., Makarova, M., Nagahama, T., Ortega, I., Palm, M., Strong, K., Schneider, M., Smale, D., Sussmann, R., and Zhou, M.: Global decadal measurements of methanol, ethene, ethyne, and HCN from the Cross-track Infrared Sounder, *Atmos. Meas. Tech.*, 18, 695–716, <https://doi.org/10.5194/amt-18-695-2025>, 2025.

Wesely, M. L., Parameterization of surface resistances to gaseous dry deposition in regional-scale numerical models, *Atmos. Environ.*, 23, 1293–1304, [https://doi.org/10.1016/0004-6981\(89\)90153-4](https://doi.org/10.1016/0004-6981(89)90153-4), 1989.

Whitburn, S., Clarisse, L., Crapeau, M., August, T., Hultberg, T., Coheur, P. F., and Clerbaux, C.: A CO₂-independent cloud mask from Infrared Atmospheric Sounding Interferometer (IASI) radiances for climate applications, *Atmos. Meas. Tech.*, 15, 6653–6668, <https://doi.org/10.5194/amt-15-6653-2022>, 2022.

Williams, J., Holzinger, R., Gros, V., Xu, X., Atlas, E., and Wallace, D. W. R.: Measurements of organic species in air and seawater from the tropical Atlantic, *Geophys. Res. Lett.*, 31, L23S06, <https://doi.org/10.1029/2004GL020012>, 2004.

Wisthaler, A., Hansel, A., Dickerson, R. R., and Crutzen, P. J.: Organic trace gas measurements by PTR-MS during INDOEX 1999, *J. Geophys. Res. Atmos.*, 107, <https://doi.org/10.1029/2001jd000576>, 2002.

Wizenberg, T., Strong, K., Jones, D. B. A., Hannigan, J. W., Ortega, I., and Mahieu, E.: Measured and modeled trends of seven tropospheric pollutants in the high Arctic from 1999 to 2022, *J. Geophys. Res.*, 129, e2023JD040544, <https://doi.org/10.1029/2023JD040544>, 2024.

Wofsy, S. C., Afshar, S., Allen, H. M., Apel, E., Asher, E. C., Barletta, B., Bent, J., Bian, H., Biggs, B. C., Blake, D. R., Blake, N., Bourgeois, I., Brock, C. A., Brune, W. H., Budney, J. W., Bui, T. P., Butler, A., Campuzano-Jost, P., Chang, C. S., Chin, M., Commane, R., Correa, G., Crounse, J. D., Cullis, P. D., Daube, B. C., Day, D. A., Dean-Day, J. M., Dibb, J. E., DiGangi, J. P., Diskin, G. S., Dollner, M., Elkins, J. W., Erdesz, F., Fiore, A. M., Flynn, C. M., Froyd, K., Gesler, D. W., Hall, S. R., Hanisco, T. F., Hannun, R. A., Hills, A. J., Hintsa, E. J., Hoffman, A., Hornbrook, R. S., Huey, L. G., Hughes, S., Jimenez, J. L., Johnson, B. J., Katich, J. M., Keeling, R. F., Kim, M. J., Kupc, A., Lait, L. R., Lamarque, J.-F., Liu, J., McKain, K., McLaughlin, R. J., Meinardi, S., Miller, D. O., Montzka, S. A., Moore, F. L., Morgan, E. J., Murphy, D. M., Murray, L. T., Nault, B. A., Neuman, J. A., Newman, P. A., Nicely, J. M., Pan, X., Paplawsky, W., Peischl, J., Prather, M. J., Price, D. J., Ray, E., Reeves, J. M., Richardson, M., Rollins, A. W., Rosenlof, K. H., Ryerson, T. B., Scheuer, E., Schill, G. P., Schroder, J. C., Schwarz, J. P., St. Clair, J. M., Steenrod, S. D., Stephens, B. B., Strode, S. A., Sweeney, C., Tanner, D., Teng, A. P., Thames, A. B., Thompson, C. R., Ullmann, K., Veres, P. R., Vieznor, N., Wagner, N. L., Watt, A., Weber, R., Weinzierl, B., Wennberg, P., Williamson, C. J., Wilson, J. C., Wolfe, G. M., Woods, C. T., and Zeng, L. H.: ATom: Merged Atmospheric Chemistry, Trace Gases, and Aerosols, ORNL DAAC, Oak Ridge, Tennessee, USA, <https://doi.org/10.3334/ORNLDAC/1581>, 2018.



Wohlfahrt, G., Amelynck, C., Ammann, C., Arneth, A., Bamberger, I., Goldstein, A. H., Gu, L., Guenther, A., Hansel, A., Heinesch, B., Holst, T., Hörtnagel, L., Karl, T., Laffineur, Q., Neftel, A., McKinney, K., Munger, J. W., Pallardy, S. G., Schade, G. W., Seco, R., and Schoon, N.: An ecosystem-scale perspective of the net land methanol flux: synthesis of micrometeorological flux measurements, *Atmos. Chem. Phys.*, 15, 7413–7427, <https://doi.org/10.5194/acp-15-7413-2015>, 2015.

1120 Yamanouchi, S., Conway, S., Strong, K., Colebatch, O., Lutsch, E., Roche, S., Taylor, J., Whaley, C. H., and Wiacek, A.: Network for the Detection of Atmospheric Composition Change (NDACC) Fourier transform infrared (FTIR) trace gas measurements at the University of Toronto Atmospheric Observatory from 2002 to 2020, *Earth Syst. Sci. Data*, 15, 3387–3418, <https://doi.org/10.5194/essd-15-3387-2023>, 2023.

1125 Yuan, H., Dai, Y., Xiao, Z., Ji, D., and Shangguan, W.: Reprocessing the MODIS Leaf Area Index products for land surface and climate modelling, *Remote Sens. Environ.*, 115, 1171–1187, <https://doi.org/10.1016/j.rse.2011.01.001>, 2011.

Zhai, S., Jacob, D. J., Franco, B., Clarisse, L., Coheur, P., Shah, V., Bates, K. H., Lin, H., Sulprizio, M. P., Huey, G., Moore, F. L., Jaffe, D. A., and Liao, H. Transpacific transport of Asian peroxyacetyl nitrate (PAN) observed from satellite: Implications for ozone, *Environ. Sci. Technol.*, 58, 9760—9769, <https://doi.org/10.1021/acs.est.4c01980>, 2024.

1130 Zhang, L., Moran, M. D., Makar, P. A., Brook, J. R., and Gong, S.: Modelling gaseous dry deposition in AURAMS: a unified regional air-quality modelling system, *Atmos. Environ.*, 36, 537–560, [https://doi.org/10.1016/S1352-2310\(01\)00447-2](https://doi.org/10.1016/S1352-2310(01)00447-2), 2002.

Zhang, L., Brook, J. R., and Vet, R.: A revised parameterization for gaseous dry deposition in air-quality models, *Atmos. Chem. Phys.*, 3, 2067–2082, <https://doi.org/10.5194/acp-3-2067-2003>, 2003.

1135 Zhu, L., Jacob, D. J., Kim, P. S., Fisher, J. A., Yu, K., Travis, K. R., Mickley, L. J., Yantosca, R. M., Sulprizio, M. P., De Smedt, I., González Abad, G., Chance, K., Li, C., Ferrare, R., Fried, A., Hair, J. W., Hanisco, T. F., Richter, D., Scarino, A. J., Walega, J., Weibring, P., and Wolfe, G. M.: Observing atmospheric formaldehyde (HCHO) from space: validation and intercomparison of six retrievals from four satellites (OMI, GOME2A, GOME2B, OMPS) with SEAC⁴RS aircraft observations over the southeast US, *Atmos. Chem. Phys.*, 16, 13477–13490, <https://doi.org/10.5194/acp-16-13477-2016>, 2016.